

THE MASSIVE SURVEY IX: PHOTOMETRIC ANALYSIS OF 35 HIGH MASS EARLY-TYPE GALAXIES WITH *HST* WFC3/IR¹

CHARLES F. GOULLAUD

Department of Physics, University of California, Berkeley, CA, USA; goullaud@berkeley.edu

JOSEPH B. JENSEN

Utah Valley University, Orem, UT, USA

JOHN P. BLAKESLEE

Herzberg Astrophysics, Victoria, BC, Canada

CHUNG-PEI MA

Department of Astronomy, University of California, Berkeley, CA, USA

JENNY E. GREENE

Princeton University, Princeton, NJ, USA

JENS THOMAS

Max Planck-Institute for Extraterrestrial Physics, Garching, Germany.

Draft version June 21, 2021

ABSTRACT

We present near-infrared observations of 35 of the most massive early-type galaxies in the local universe. The observations were made using the infrared channel of the *Hubble Space Telescope* (*HST*) *Wide Field Camera 3* (WFC3) in the F110W (1.1 μm) filter. We measured surface brightness profiles and elliptical isophotal fit parameters from the nuclear regions out to a radius of ~ 10 kpc in most cases. We find that 37% (13) of the galaxies in our sample have isophotal position angle rotations greater than 20° over the radial range imaged by WFC3/IR, which is often due to the presence of neighbors or multiple nuclei. Most galaxies in our sample are significantly rounder near the center than in the outer regions. This sample contains six fast rotators and 28 slow rotators. We find that all fast rotators are either diskly or show no measurable deviation from purely elliptical isophotes. Among slow rotators, significantly diskly and boxy galaxies occur with nearly equal frequency. The galaxies in our sample often exhibit changing isophotal shapes, sometimes showing both significantly diskly and boxy isophotes at different radii. The fact that parameters vary widely between galaxies and within individual galaxies is evidence that these massive galaxies have complicated formation histories, and some of them have experienced recent mergers and have not fully relaxed. These data demonstrate the value of high spatial resolution IR imaging of galaxies and provide measurements necessary for determining stellar masses, dynamics, and black hole masses in high mass galaxies.

Keywords: galaxies: elliptical and lenticular, cD — galaxies: photometry — galaxies: structure

1. INTRODUCTION

Massive early-type galaxies are the modern-day remnants of the earliest major star-formation events in the history of the universe, and they comprise a substantial fraction of the stellar mass in the local universe (e.g., Renzini 2006). Thus, understanding the formation histories of such galaxies is central to the problem of galaxy formation in general. The MASSIVE survey, described by Ma et al. (2014, Paper I), is an ongoing systematic effort using integral field spectroscopy and other data to

study the detailed mass structure and abundance profiles of the highest mass galaxies in the local universe. The complete MASSIVE sample includes all early-type galaxies in the northern sky out to an estimated distance of 108 Mpc and absolute K -band magnitude $M_K < -25.3$ mag, corresponding to stellar masses $M_* \gtrsim 10^{11.5} M_\odot$.

In Paper II of the MASSIVE survey, Greene et al. (2015) presented the first results on stellar population gradients from spatially resolved absorption line measurements and found evidence that the centers of massive galaxies formed rapidly at high redshift, while the outskirts were accreted during later mergers. Davis et al. (2016, Paper III) presented a pilot study of CO observations in 15 MASSIVE galaxies and found a significant amount of cold gas in ten of the galaxies. Paper IV (Goulding et al. 2016) used archival Chandra X-

¹Based on observations with the NASA/ESA *Hubble Space Telescope*, obtained at the Space Telescope Science Institute, which is operated by the Association of Universities for Research in Astronomy, Inc., under NASA contract NAS 5-26555. These observations are associated with Program GO-14219.

ray images to analyze the hot X-ray gas properties in 33 MASSIVE galaxies and additional lower mass galaxies from the ATLAS^{3D} survey (Cappellari et al. 2011). Paper V (Veale et al. 2017b) presented stellar kinematics for the subset of 41 MASSIVE galaxies with stellar masses $M_* \gtrsim 10^{11.8} M_\odot$, and Paper VI (Pandya et al. 2017) studied the spatial distribution and kinematics of the warm ionized gas. Paper VII (Veale et al. 2017a) presented integral field spectroscopic measurements of the specific spin parameter λ_e in a complete mass-limited subsample of 75 MASSIVE galaxies, and examined the interrelationships between λ_e , stellar mass, and environment in a combined sample of 370 MASSIVE and ATLAS^{3D} survey galaxies. Velocity dispersion profiles for 90 MASSIVE galaxies out to projected radii as large as 30 kpc were presented in Paper VIII (Veale et al. 2018), which found strong evidence for a trend in the outer slope of the dispersion profile with environment.

All of the MASSIVE studies to date have been based primarily on optical or radio-wavelength spectroscopic observations or archival X-ray data. However, photometric imaging data are also an essential element of the MASSIVE project for determining the stellar mass profiles of the sample galaxies. An important goal of the project is to constrain the central supermassive black hole (SMBH) masses M_{BH} in MASSIVE galaxies using Schwarzschild orbit modeling (Thomas et al. 2004). Multiple mass components contribute to the gravitational potential to varying degrees as a function of galactocentric radius, and an individual star may travel from the sphere of influence of the SMBH to large radii where dark matter dominates, traversing the intermediate region dominated by the stellar mass. Therefore, in order to disentangle the contributions of the various components and construct stellar orbits in the combined gravitational potential, the dynamical models require accurate characterization of the stellar luminosity profile from the galaxy center to its outskirts. In particular, the derived SMBH mass is partly degenerate with the central stellar mass profile; the inner luminosity profile and stellar mass-to-light ratio must be well constrained in order to obtain a robust measurement of M_{BH} . For example, Thomas et al. (2016) used archival *Hubble Space Telescope* (*HST*) NICMOS imaging to constrain the very flat core in NGC 1600 and dynamically determined $M_{\text{BH}} = (1.7 \pm 0.15) \times 10^{10} M_\odot$, the largest SMBH known in the local universe outside a rich galaxy cluster. We have been amassing new and archival high-resolution *HST* and wide-field ground-based photometry for the full sample of MASSIVE galaxies to better understand their stellar and central black hole masses.

HST has revolutionized the study of early-type galaxies, especially with regard to the complex properties of their central regions. Ferrarese et al. (1994) studied a sample of 14 early-type galaxies in the Virgo cluster and found that they fell into two groups: those whose surface brightness profiles became less steep near their centers and were best fit by a broken power-law (“core” galaxies), and those whose interiors were well described by a single logarithmic slope (“power-law” galaxies). Based on a larger, but more heterogeneous, sample of 45 galaxies, Lauer et al. (1995) came to a similar conclusion and fitted all the profiles with a double power-law model (dubbed the “Nuker law”) that included a transition sharpness parameter. Their results showed a clear bimodality in

the value of the logarithmic slope γ inside the break (or transition) radius, with core galaxies having $\gamma < 0.3$ and power-law galaxies having $\gamma \gtrsim 0.6$; very few galaxies in their sample had γ between these two ranges (Laine et al. 2003; Lauer et al. 2005, 2007).

Faber et al. (1997) studied a somewhat larger sample and demonstrated that the central slope correlates strongly with luminosity: luminous galaxies (those with $M_V < -22$) possessed central cores, while faint galaxies with $M_V > -20$ had power-law profiles over the range of radii explored. Intermediate luminosity galaxies occupied a transition region with a mix of power-law and core profiles. Laine et al. (2003) observed 81 brightest cluster galaxies with *HST* and came to the conclusion that the distribution of core and power-law profiles is bimodal, a result supported by Lauer et al. (2007). On the other hand, other studies have shown that the transition in central slope from power-law to core occurs smoothly with galaxy luminosity, or stellar mass (Graham et al. 2003; Ferrarese et al. 2006; Côté et al. 2007; Glass et al. 2011). The more recent studies tend to parameterize early-type galaxy profiles using Sérsic (Sérsic 1968) or core-Sérsic (Graham et al. 2003) profiles, and associate the difference between these two profiles for a given galaxy as representing the amount of “missing,” or depleted, stellar mass at their centers (e.g., Trujillo et al. 2004; Ferrarese et al. 2006; Kormendy et al. 2009; Rusli et al. 2013). Thomas et al. (2016) demonstrated that the break radius in the core-Sérsic fit to a galaxy profile corresponds closely to the radius of the sphere of influence of the central SMBH. Thus, a single high-resolution photometric measurement can provide a reasonable prediction of M_{BH} for massive galaxies. The aim of this paper is not to address the core/cusp issue, but to explore the photometric properties of the MASSIVE galaxies outside the nuclear regions to constrain the stellar mass distributions in preparation for accurate black hole mass and SBF distance measurements.

While the studies above focused on the surface brightness profiles of the nuclear regions of the galaxies, others have used the shapes of the isophotes to study the structure and formation histories of early-type galaxies. These measurements include ellipticity, position angle (PA) rotation, isophote center shifts, and deviations from purely elliptical isophotes (i.e., diskiness or boxiness; Franx et al. 1989; Kormendy & Bender 1996). For example, attempts to determine the intrinsic shapes of galaxies from the statistical frequency distribution of observed projected ellipticities have suggested that the brightest elliptical galaxies must be intrinsically triaxial, compared to lower-luminosity early-type galaxies, which appear to be axisymmetric (e.g., Tremblay & Merritt 1996; Vincent & Ryden 2005). Likewise, kinematic misalignments, which cannot occur in axisymmetric systems, are more frequent in more massive galaxies (e.g., Emsellem et al. 2007).

Indeed, to explain the global photometric and kinematic structure of elliptical galaxies, a rough paradigm has emerged where high-mass galaxies primarily form in gas poor merging situations which produce boxy, anisotropic, cored, triaxial giant ellipticals; lower-mass elliptical galaxies preferentially form from the gas rich mergers of disk galaxies that produce rotating, disk ellipticals (Ferrarese et al. 1994; van den Bosch et al. 1994;

Lauer et al. 1995; Kormendy & Bender 1996; Rest et al. 2001; Lauer et al. 2005; Ferrarese et al. 2006). More specifically, Weijmans et al. (2014), for example, suggested that angular momentum is the crucial parameter and that the fast rotators make the flatter and nearly axisymmetric elliptical galaxy subpopulation, while the statistically less flattened and triaxial ones are slow rotators. This was based on the ATLAS^{3D} sample, which lacks the most massive (predominantly slow rotator) galaxies targeted by MASSIVE, for which we present new data here.

For individual galaxies, photometric data alone are not sufficient to constrain the intrinsic axis ratios. They must be complemented by stellar kinematics and detailed dynamical modeling (e.g., Statler 1994; Magorrian 1999; Gerhard & Binney 1996). However, some clues on the intrinsic shape of a galaxy are directly encoded in the isophotes. PA rotation measurements, for example, provide a lower limit for the statistical occurrence of non-axisymmetry and, hence, are an important piece of information in the context of elliptical galaxy evolution (e.g., Stark 1977; Williams & Schwarzschild 1979).

High-spatial resolution *HST* imaging has also revealed the presence of dust in the centers of many early-type galaxies. Rest et al. (2001) analyzed an unbiased, though incomplete, magnitude- and space-limited sample of 67 early-type galaxies within 54 Mpc, while Lauer et al. (2005) studied a sample of 77 galaxies within 100 Mpc using archival observations. Both studies found nuclear dust in roughly half of the galaxies. Ferrarese et al. (2006) conducted the first survey of early-type galaxies using the *Advanced Camera for Surveys* (ACS), enabling surface photometry measurements out to $\gtrsim 1.5$ arcmin, as compared to the ~ 20 arcsec limit of previous studies that only utilized the PC chip of *WFPC2*. Their study examined 100 early-type galaxies from the ACS Virgo Cluster Survey (Côté et al. 2004), with the brightest 26 galaxies forming a magnitude-limited sample, and confirmed the presence of dust in roughly half of the most massive early-type galaxies. Although this sample was much more complete and homogeneous than other studies of early-type galaxies with *HST*, the very limited volume meant that it contained only a few galaxies at masses $\gtrsim 10^{11.5} M_{\odot}$. Thus, no survey has yet included a complete sample of the most massive early-type galaxies in the local universe.

This paper presents new IR imaging observations with the Infrared Channel of the *HST* Wide Field Camera 3 (WFC3/IR) of a complete subsample of 35 galaxies selected from the MASSIVE survey (GO-14219, P.I. J. Blakeslee). The purpose of this study is to: (1) measure accurate surface brightness profiles to establish the stellar mass profiles in order to better constrain the black hole masses; and (2) to measure the radial variations in isophotal parameters to test the idea that the most massive galaxies are preferentially boxy and slowly rotating. The high-resolution IR imaging data of this sample of MASSIVE galaxies provides detailed insight into the structures and formation histories of these galaxies that goes beyond a simplistic characterization of each galaxy. We analyze the radial variation of isophote center, position angle, ellipticity, and boxiness or diskiness for each galaxy, and we examine possible trends among various mean isophotal parameters as a function of radius out to ~ 10 kpc. We also discuss the prevalence and distribution

of central dust in our sample galaxies and highlight the peculiar double nucleus in the galaxy NGC 1129.

The following section describes the observations and data reduction procedures, background sky estimation, mask construction, and the isophotal fitting process we used to measure the surface brightness profiles. Sec. 3 presents our surface brightness profile measurements, which are shown in detail for each galaxy in the Appendix along with IR images of each galaxy. Sec. 4 summarizes our results that provide a unique look into the photometric properties of the most massive early-type galaxies, a population that has not been systematically studied prior to the MASSIVE survey. Distances for our sample galaxies, measured using the surface brightness fluctuations method, will be reported in a subsequent paper.

2. INFRARED IMAGING

2.1. Observations and Data Reduction

The current sample of 35 galaxies was selected from among the nearest of the 72 most luminous MASSIVE galaxies, and includes all the early-type MASSIVE galaxies within 80 Mpc for which surface brightness fluctuation (SBF) distances can be measured in a single orbit (Jensen et al. 2015). Accurate distances are key to measuring the black hole–galaxy mass relationship, as well as determining the dynamical properties of the galaxy. The current sample is limited to those MASSIVE galaxies for which accurate SBF distances are feasible and currently unavailable in the literature. Each galaxy was observed for one orbit using the F110W filter (Table 1). This paper reports the results of our surface brightness profile measurements and the galaxy structural properties derived from them.

Each orbit was divided into five dithered exposures (four galaxies received an additional shorter exposure when it could be scheduled during the orbit). Two galaxies (NGC 545 and NGC 547) were observed simultaneously. The total exposure time for each galaxy is listed in Table 1. The dithered exposures used a five point sub-pixel dither pattern to improve sampling of the point-spread function (PSF); the pixel scale at F110W is 0.128 arcsec pix^{-1} , which is slightly undersampled for this wavelength. Properties for each galaxy can be found in Table 1.

The WFC3/IR images were first reduced using the standard data reduction pipeline, as outlined in the STScI data handbook for WFC3/IR.² Approximately 40% of the individual F110W exposures were affected by the diffuse upper-atmosphere He emission line at $1.083 \mu\text{m}$ (Brammer et al. 2014), resulting in an elevated background. During each MULTIACCUM exposure, multiple nondestructive reads of the detector were saved, allowing us to determine the rate at which signal accumulated in each pixel and therefore identify pixels that were affected by saturation or cosmic rays, which could be identified as a change in the count rate of electrons being detected in a pixel. The He emission, which appears as a variable background, also causes the signal rate to change nonlinearly during an individual MULTIACCUM exposure.

² http://www.stsci.edu/hst/wfc3/pipeline/wfc3_pipeline

Table 1
Properties for Observed Galaxies

Galaxy (1)	R.A. (deg) (2)	Dec. (deg) (3)	D (Mpc) (4)	M_K (mag) (5)	A_V (mag) (6)	Exposure (sec) (7)	Background (mag arcsec ⁻²) (8)	Background (e ⁻ s ⁻¹ pix ⁻¹) (9)
NGC 0057	003.8787	17.3284	76.3	-25.75	0.212	2496	22.00	1.39 ± 0.08
NGC 0315	014.4538	30.3524	70.3	-26.30	0.177	2496	21.77	1.72 ± 0.23
NGC 0383	016.8540	32.4126	71.3	-25.81	0.194	2496	21.94	1.47 ± 0.11
NGC 0410	017.7453	33.152	71.3	-25.90	0.161	2496	21.62	1.98 ± 0.07*
NGC 0507	020.9164	33.2561	69.8	-25.93	0.170	2496	21.56	2.08 ± 0.16*
NGC 0533	021.3808	1.759	77.9	-26.05	0.084	2496	21.50	2.21 ± 0.08
NGC 0545	021.4963	-1.3402	74.0	-25.83	0.114	2496	21.85	1.59 ± 0.06
NGC 0547	021.5024	-1.3451	74.0	-25.83	0.113	2496	21.85	1.59 ± 0.06
NGC 0665	026.2338	10.423	74.6	-25.51	0.242	2496	21.79	1.69 ± 0.08
NGC 0708	028.1937	36.1518	69.0	-25.65	0.247	2496	21.84	1.61 ± 0.08
NGC 0741	029.0874	5.6289	73.9	-26.06	0.144	2496	21.81	1.65 ± 0.12
NGC 0777	030.0622	31.4294	72.2	-25.94	0.128	2496	21.79	1.69 ± 0.08
NGC 0890	035.5042	33.2661	55.6	-25.50	0.212	2496	21.94	1.47 ± 0.20*
NGC 1016	039.5815	2.1193	95.2	-26.33	0.085	2496	21.72	1.80 ± 0.14
NGC 1060	040.8127	32.425	67.4	-26.00	0.532	2496	21.74	1.77 ± 0.15
NGC 1129	043.6141	41.5796	73.9	-26.14	0.309	2496	21.53	2.15 ± 0.09
NGC 1167	045.4265	35.2056	70.2	-25.64	0.496	2496	21.71	1.82 ± 0.08*
NGC 1272	049.8387	41.4906	77.5	-25.80	0.441	2496	21.87	1.57 ± 0.04
NGC 1453	056.6136	-3.9688	56.4	-25.67	0.289	2496	21.65	1.92 ± 0.16
NGC 1573	068.7666	73.2624	65.0	-25.55	0.377	2895	21.06	3.29 ± 0.14*
NGC 1600	067.9161	-5.0861	63.8	-25.99	0.118	2496	21.78	1.70 ± 0.19*
NGC 1684	073.1298	-3.1061	63.5	-25.34	0.159	2496	21.83	1.62 ± 0.08
NGC 1700	074.2347	-4.8658	54.4	-25.60	0.119	2496	21.91	1.51 ± 0.18
NGC 2258	101.9425	74.4818	59.0	-25.66	0.351	2895	21.32	2.60 ± 0.12*
NGC 2274	101.8224	33.5672	73.8	-25.69	0.286	2496	21.83	1.62 ± 0.19*
NGC 2513	120.6028	9.4136	70.8	-25.52	0.063	2496	21.50	2.21 ± 0.06*
NGC 2672	132.3412	19.075	61.5	-25.60	0.058	2496	21.66	1.90 ± 0.19
NGC 2693	134.2469	51.3474	74.4	-25.76	0.054	2695	21.92	1.50 ± 0.26*
NGC 4914	195.1789	37.3153	74.5	-25.72	0.037	2496	22.30	1.05 ± 0.08
NGC 5322	207.3133	60.1904	34.2	-25.51	0.038	2745	21.32	2.60 ± 0.20
NGC 5353	208.3613	40.2831	41.1	-25.45	0.035	2496	21.72	1.80 ± 0.21
NGC 5557	214.6071	36.4936	51.0	-25.46	0.016	2496	21.92	1.49 ± 0.08*
NGC 6482	267.9534	23.0719	61.4	-25.60	0.277	2496	22.41	0.95 ± 0.04
NGC 7052	319.6377	26.4469	69.3	-25.67	0.337	2496	22.36	1.00 ± 0.28
NGC 7619	350.0605	8.2063	54.0	-25.65	0.224	2496	21.58	2.05 ± 0.06

Note. — Column (1) galaxy name. Column (2) right ascension in degrees (J2000.0). Column (3) declination in degrees (J2000.0). Column (4) redshift distances from Ma et al. (2014). NGC 1016 is included in this sample because it has Tully-Fisher and D_n - σ distances near ~ 80 Mpc (Theureau et al. 2007; Willick et al. 1997), which is significantly lower than the group redshift distance tabulated here. Column (5) extinction-corrected total absolute K -band magnitude from Ma et al. (2014). Column (6) foreground galactic extinction in Landolt V -band (Schlafly & Finkbeiner 2011) with reddening relation of Fitzpatrick (1999). Column (7) total exposure time in seconds. Column (8) background value, determined in Section 2.2. Column (9) background value in the native WFC3/IR resolution. Starred galaxies were affected by the variable He emission background.

Each raw image was run through a specialized Python program³ written by Gabriel Brammer at STScI to correct for variable background levels and other events in MULTIACCUM sequences (like satellite passages) that affected the flux in a large number of pixels at once. The correction algorithm starts by comparing the count rate over a large region of the detector in the first and last reads of a MULTIACCUM sequence, and then flattens the sequence of reads so that each individual subframe has the same average background count rate. We used Brammer’s program to identify individual subframes that had varying background and re-processed all images to have flattened (linear) background count rates. This process does not adjust the median sky level, so some background values are still higher than would otherwise be expected in the absence of the elevated He background (see Table 1). The individual exposures were then combined using the STSDAS PyRAF task *Astro-drizzle*. During stacking, we rescaled our images from

the native 0.128 arcsec pix⁻¹ to 0.10 arcsec pix⁻¹ to improve spatial resolution, which is possible due to the fractional-pixel offsets of the dither pattern. The following parameters were changed from their default values in order to rescale the final images:

```

skywidth           = 0.1           skystat           = mode
dirz_sep_kernel   = square        dirz_sep_bits     = 4928
combine_maskpt    = 0.7           combine_type      = median
driz_cr_corr      = True           driz_cr_snr      = 10.0 8.0
final_kernel      = gaussian      final_pixfrac     = 0.6
final_bits        = 4928          final_wcs         = True
final_scale       = 0.10

```

2.2. Background Measurements

The MASSIVE galaxies in our sample are extended enough that, in most cases, the entire field of view contained light from the galaxy that was a significant fraction of the instrumental background. As a conse-

³ <https://github.com/gbrammer/wfc3>

quence, the standard background subtraction procedure performed by *Astrodrizzle*, which is based on the median value in the field of view, oversubtracted the sky. In order to accurately measure the surface brightness profiles of each galaxy, we iteratively compared our measured profiles using different background offsets to $r^{1/4}$ models, Sersic profiles from the NASA-Sloan Atlas⁴ (NSA), and empirical Two Micron All-Sky Survey (2MASS) J -band profiles.

A first background estimate was made by measuring the median value in the darkest corners of each image. This value provided an absolute upper limit on the background value and provided an initial background estimate. We then created our initial elliptical model of each galaxy using two different programs, ELLIPSE and ELLIPROF. Each program determined the surface brightness profile in annuli that were allowed to vary in ellipticity, ellipse center, and PA. ELLIPSE utilizes the fitting framework outlined by Carter (1978), and later modified for full isophote fitting by Jedrzejewski (1987). The intensity profile model $I(\phi)$ is constructed from the mean intensity $\langle I_{ell} \rangle$ along an elliptical path with Fourier series azimuthal perturbations along the elliptical path:

$$I(\phi) = \langle I_{ell} \rangle + \sum_n (a_n \sin(n\phi) + b_n \cos(n\phi)) \quad (1)$$

where ϕ is the azimuthal angle. ELLIPSE fits the purely elliptical patterns first by minimizing the residual between the model and data. Higher order deviations are fitted sequentially. We also utilized the galaxy isophote modeling task ELLIPROF (Tonry et al. 1997; Jordán et al. 2004). ELLIPROF is similar to ELLIPSE but provides an independent comparison for testing the robustness of the fit parameters. It also provides an extrapolation beyond the outer annulus, which is convenient for situations where a sharp cut-off in the model is undesirable, such as in the iterative fitting of multiple galaxies in the field of view. Many galaxies have nearby neighbors in the frame, which frequently skewed the isophotal fits. To correct for bright companions, we used ELLIPROF to iteratively fit each galaxy until the residuals after galaxy subtraction were minimized within the field of view. Stars and other bright objects in the frame were masked prior to fitting with ELLIPROF.

The surface brightness profiles were then compared to Sersic and $r^{1/4}$ models to determine the residual sky background, assuming that the galaxies follow a Sersic or $r^{1/4}$ distribution. The Sersic profiles were fitted to the outer ten isophotes of the surface brightness profile with the intensity as the only free variable. The $r^{1/4}$ profiles were fitted with both the effective radius r_e and intensity as free variables. The background estimate adopted for each iteration and for each profile was that for which the residuals were minimized. This procedure was performed independently by two members of our collaboration, one using ELLIPSE and the other using ELLIPROF, to determine the background levels.

As a third independent measurement of the background, we compared our F110W surface brightness profiles to 2MASS J -band images (Jarrett et al. 2000).⁵ The

2MASS profiles were measured in a comparable way to our F110W profiles in elliptical annuli after subtracting the sky value determined much farther from the galaxies than is possible in the WFC3/IR images. Generally speaking, the F110W and 2MASS J -band profiles agree very well. In some cases the profiles were offset from one another, usually when bright companion galaxies affected the surface brightness profiles. The procedure for removing companions from the 2MASS images was to automatically identify and mask objects using SExtractor (Bertin & Arnouts 1996), which was less effective when companions were large and close.

The final background measurements and their uncertainties were adopted after carefully considering both the comparison with 2MASS surface brightness profiles and the background levels that we found from Sersic and $r^{1/4}$ extrapolations. The Sersic, $r^{1/4}$, and 2MASS profiles all had their own uncertainties associated with their best fits. To determine the best background value, we adopted the preferred value from the Sersic or $r^{1/4}$ profile, depending on which was the closest fit to the surface brightness profile. In 17 cases, the $r^{1/4}$ profile was either the better or only fit available. The process of determining the best background level involved the following criteria:

1. If the Sersic or $r^{1/4}$ profile background measurement was within the 2MASS profile's uncertainty range, the Sersic or $r^{1/4}$ fit value for the background was adopted (17 galaxies).
2. If the Sersic or $r^{1/4}$ profile background measurement was outside the 2MASS profile's uncertainty range, the background value was increased or decreased until it fell within the uncertainty range of both fits (12 galaxies).
3. In cases where a bright companion was present, the 2MASS profile was disregarded when determining the background value. Instead, the value was solely determined by the profile fits to the WFC3/IR images (four galaxies).
4. If the background measurement found in the corner of the image was lower than the value determined through the system above, the corner value was adopted, as this value functioned as a boundary condition on our background measurements (two galaxies).

The scatter in the different estimates of the instrumental background served as a measurement of the uncertainty (see Table 1). The adopted sky levels were then applied to the final stacked images from *Astrodrizzle* before measuring the final surface brightness profiles. The mean background level we measured for this sample was $1.78 \pm 0.18 \text{ e}^- \text{ s}^{-1} \text{ pix}^{-1}$ for the native WFC3/IR average pixel scale ($0.128 \text{ arcsec pix}^{-1}$), or $21.77 \pm 0.11 \text{ AB mag arcsec}^{-2}$. The uncertainty for each background measurement was estimated by calculating the standard deviation of four independent background measurements: the value derived from the 2MASS J -band profile, the NSA Sersic value, and two independent $r^{1/4}$ profile values (the first using the $0.10 \text{ arcsec pix}^{-1}$ *Astrodrizzle* images and ELLIPSE, and the other using the images in the

⁴ <http://www.nsatlas.org>

⁵ 2MASS profiles were kindly provided by John Lucey.

original 0.128 arcsec pix^{-1} resolution with no geometric distortion correction and ELLIPROF). In eight cases, the standard deviation was high due to an outlier in the four independent measurements. These cases were recalculated without the outlier (though the outlier was still considered when determining the background measurement itself). In five cases, the standard deviation was lower than expected based on the empirical estimates of the uncertainty from the $r^{1/4}$ fits (which were performed first), often in cases where one of the independent measurements had been excluded as an outlier. In these cases the empirical uncertainty was used instead of the standard deviation. Overall, the average uncertainty for our background measurements is $0.13 \text{ e}^{-\text{s}^{-1}\text{pix}^{-1}}$ in the native 0.128 arcsec pix^{-1} resolution. This compares favorably with the standard deviation of the differences between the different background estimates, or $0.11 \text{ e}^{-\text{s}^{-1}\text{pix}^{-1}}$. The variation in background levels between different observations is $0.5 \text{ e}^{-\text{s}^{-1}\text{pix}^{-1}}$. These values are consistent with the published range of values for WFC3/IR from zodiacal light (Pirzkal 2014) and the He emission. Final estimated background levels are listed in Table 1.

2.3. Neighbor Subtraction

Many of the target galaxies have nearby neighbors in the field of view. Due to their size and position, these galaxies could not be masked without significantly distorting the final surface brightness profile fits. Instead, we iteratively modeled these galaxies using ELLIPROF. An initial model for the main galaxy was created and subtracted before fitting the neighbor galaxy. The model of the neighbor galaxy was then subtracted from the original image, and the target galaxy fitted again. This procedure was repeated until the models for both galaxies converged and the residual structure in the background was minimized. Although we used PyRAF’s ELLIPSE and BMODEL for fitting the final surface brightness profiles and generating the models, we found that ELLIPROF did a much better job with the iterative fitting of multiple galaxies because, unlike ELLIPSE, it extrapolates the galaxy models to the full field of view. The iterative fitting of neighbor galaxies was performed both as part of the measurement of the instrumental background and the final surface brightness measurements of the target galaxies.

2.4. Mask Creation

After the background values were measured and any neighbor galaxy models generated, we subtracted both from the images and created masks for other objects in the field of view. Due to the size of the galaxies, we required an iterative procedure to identify and mask sources within the bright interior of each galaxy. The first iteration of the mask was generated by using the CTX image extension produced by *Astrodrizzle*, which identifies bad pixels in the image. Next, we fed the mask and residual image R_0 (the image with background and nearby neighbors subtracted) into SExtractor (Bertin & Arnouts 1996) to detect objects in the image. The first SExtractor iteration was used to identify large, bright objects in the outer regions of the galaxy image. SExtractor identified an object if at least six contiguous pixels deviated from the median grid value by more than

4σ . Since the center of the galaxy was always identified as an object, no objects within 5 arcsec of the center were masked. All remaining pixels were combined with the previous iteration of the mask to form the new residual image. ELLIPSE was then run on the image with the SExtractor objects masked, generating a set of isophotes that were used by the PyRAF task BMODEL to create a model galaxy image. BMODEL does not generate values outside the largest fitted isophote, so we extrapolated the model by fitting a power law to the outer five isophotes. The new galaxy model was then subtracted from the initial residual image to form an updated residual image R_1 for subsequent object identification and masking.

Next, we fed the R_1 residual image and mask into SExtractor a second time, this time with the goal of identifying bright extended sources closer to the target galaxy center that were missed during the first SExtractor run. For the second iteration, the detection threshold was set at 11σ , and the minimum area was held at six pixels. Objects found within 5 arcsec of the center were ignored to prevent the center of the galaxy from being masked. Objects masked by this iteration were added to the previous mask to create the penultimate version.

The new mask was used to create an updated galaxy model and residual image R_2 , which was analyzed with SExtractor a final time. With the brightest sources in the interior masked, the galaxy model was finally good enough so that fainter point sources close to the galaxy center could be identified. We set the SExtractor detection threshold to 4σ and the minimum object area to five pixels, and objects within 5 arcsec of the galaxy center were ignored. The last iteration of masking could introduce erroneous masking around the edge of the largest isophote fitted by ELLIPSE. To avoid this, we combined the first and last iterations of the mask; the first iteration was used for the region outside the largest isophote, and the last iteration was used for the region within. Finally, to make sure we masked all the light from the objects, we expanded the footprint of each masked object by smoothing the point source mask using a $\sigma = 0.6$ -pixel Gaussian and masking any fractional pixel values.

After the background was subtracted, neighboring galaxies removed, and the object mask created, we ran each galaxy through ELLIPSE one last time to generate a final galaxy model using BMODEL and a final residual image R_f . The galaxy images, isophotal models, and residual images are shown in Figure 1. The fourth panel in Figure 1 (and subsequent figures in the Appendix) shows the magnified central region of the original image to show the nuclear structure including dust and other central features. The isophotes were generated using CMODEL, a correction to the BMODEL task by Ciambur (2015) that correctly utilizes the higher-order moments when generating the model.

3. PHOTOMETRIC MEASUREMENTS

3.1. Surface Brightness Profiles

The surface brightness profiles fitted using ELLIPSE are shown in Figure 1 for NGC 57. The profiles and images for the other 34 galaxies can be found in the Appendix. In addition to the surface brightness profile, eight parameters are plotted for each galaxy as a function of radius that describe the shape of the isophotes: posi-

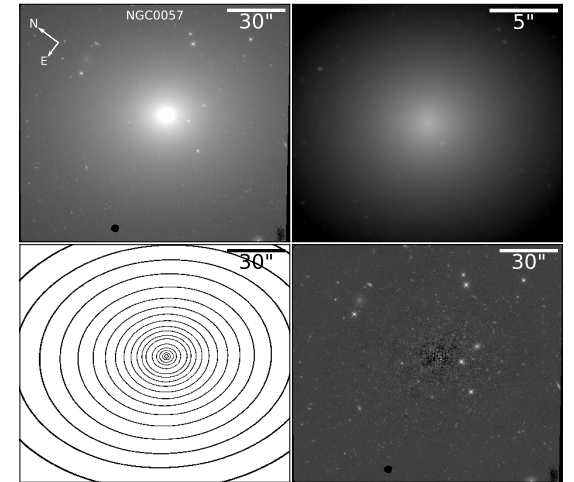
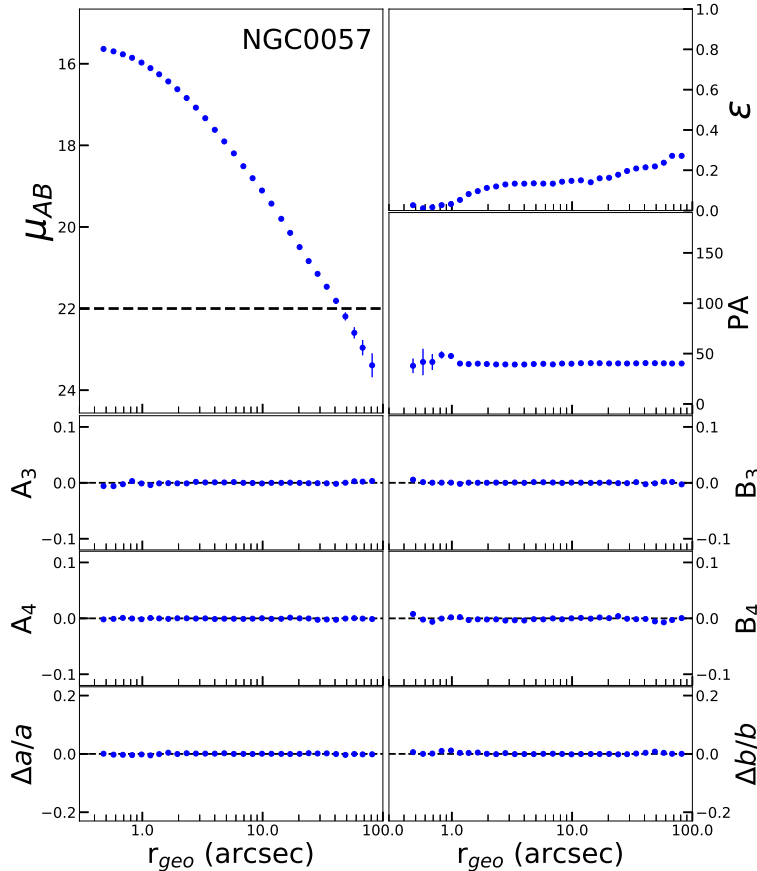


Figure 1. Images and radial plots for NGC 57. The scale is 1 arcsec = 370 pc. The images are (*Upper Left*) the F110W band image, (*Lower Left*) the isophotes derived from the surface brightness profile model (semi-major axis increases by 15% between isophotes), (*Upper Right*) a closer view of the center of the F110W image (scaled to make central features, such as dust, more visible), and (*Lower Right*) the residual image with galaxy models subtracted. The radial plots in the left panel show isophotal parameters as a function of the geometric mean radius, $r_{geo} = \sqrt{ab}$, where a is the semi-major axis and b is the semi-minor axis. The horizontal black dotted line in the surface brightness profile shows the background measurement. Radial plots and images for the remainder of the sample are displayed in the Appendix.

tion angle, ellipticity ϵ , the higher order deviations from ellipticity A_3 , B_3 , A_4 , and B_4 , and finally the isophotal drifts from the center of the galaxy along the semi-major and semi-minor axes, Δa and Δb , respectively. The higher order deviations from ellipticity used here are defined as

$$A_n = \frac{a_n}{a \nabla I}, \quad B_n = \frac{b_n}{a \nabla I} \quad (2)$$

where a_n and b_n are defined in Equation 1, ∇I is the intensity gradient at a particular isophote, and a is the semi-major axis. Intensity- and luminosity-weighted values for ellipticity, PA, and B_4 are tabulated in Table 2. In addition to overall luminosity-weighted values, the behavior of these parameters has been examined within three different radial regimes: an inner regime extending from 0.4 arcsec to $0.1r_s$, an intermediate regime extending from $0.1r_s$ to r_s , and an outer regime comprised of all points beyond r_s . The parameter $r_s = 7.5$ kpc was chosen as a representative physical scale based on typical R_e values from 2MASS and NSA fits to the galaxies in our sample.

3.2. Radial Variations of Isophotal Parameters

3.2.1. Ellipticity

In their study of early-type galaxies from the ACS Virgo Cluster Survey (ACSVCS), Ferrarese et al. (2006)

concluded that there was no trend in ellipticity with increasing stellar mass. When combined with our sample, we find that early-type galaxies are rounder at the high-mass end (Fig. 2). Both the average intensity-weighted ellipticity and the scatter in ellipticity decrease with increasing mass. Emsellem et al. (2011) found that slow rotators with $10^{11} M_\odot < M < 10^{11.5} M_\odot$ have lower ellipticities than slow rotators with $M < 10^{11} M_\odot$. Emsellem et al. (2011) connected this to an observed trend that the specific angular momentum of a slow rotator is inversely correlated with stellar mass. The observed behavior of ellipticity with stellar mass for our sample is in agreement with that of Emsellem et al. (2011), but for a sample that begins, rather than ends, at $\sim 10^{11.5} M_\odot$.

Over the radial profiles of the galaxies in this sample, isophotes tend to be rounder towards the centers of the galaxies (see Fig. 3). Only six galaxies without central dust have higher ellipticities near their centers than they do at larger radii. Of these, only one (NGC 1129) has an increase in ellipticity larger than 20% from the value at 7.5 kpc, and this increase is likely the result of ELLIPSE attempting to fit isophotes to NGC 1129's double nucleus. In contrast, 18 galaxies without central dust have rounder interior isophotes, and four galaxies (NGC 410, NGC 665, NGC 890, and NGC 2258) have a decrease in ellipticity larger than 0.20 from the value at 7.5 kpc.

Table 2
Parameter Shifts and Luminosity-weighted Values

Galaxy	r_s (arcsec)	ΔPA_{tot} (Deg)	$\langle \Delta r \rangle_L$	$\langle \epsilon \rangle_L$	$\langle PA \rangle_L$ (Deg)	$\langle B_4 \rangle_I$ $\times 100$	$\langle B_4 \rangle_L$ $\times 100$	Structural Features	Type	Group
(1)	(2)	(3)	(4)	(5)	(6)	(7)	(8)	(9)	(10)	(11)
NGC 0057	21.3	5	0.0023	0.17 ± 0.002	40.2 ± 0.5	0.055 ± 0.062	-0.095 ± 0.014		E	1
NGC 0315	22.0	7	0.0049	0.27 ± 0.001	44.3 ± 0.2	-1.1 ± 0.041	-0.95 ± 0.018	D	E	6B
NGC 0383	21.7	13	0.0045	0.19 ± 0.001	138.9 ± 0.3	0.17 ± 0.013	0.3 ± 0.013	DN	E-S0	29
NGC 0410	21.7	0	0.013	0.24 ± 0.001	35.8 ± 0.9	-0.0093 ± 0.048	0.99 ± 0.02		E	29B
NGC 0507	22.2	71	0.03	0.16 ± 0.002	52.1 ± 0.9	0.12 ± 0.049	0.4 ± 0.02		E-S0	35B
NGC 0533	19.9	10	0.0068	0.27 ± 0.001	49.3 ± 0.2	-0.097 ± 0.048	-0.013 ± 0.012		E	3B
NGC 0545	20.9	22	0.017	0.29 ± 0.002	57.2 ± 0.7	-0.4 ± 0.06	-0.072 ± 0.02	N	E-S0	35B
NGC 0547	20.9	36	0.014	0.14 ± 0.001	98.8 ± 1.4	-0.71 ± 0.099	-0.25 ± 0.019	N	E	35
NGC 0665	20.7	74	0.019	0.28 ± 0.002	102.4 ± 1.4	0.16 ± 0.053	1.2 ± 0.061	D	S0	4B
NGC 0708	22.4	82	0.018	0.32 ± 0.002	39.8 ± 0.2	0.14 ± 0.026	-0.024 ± 0.031	DN	E	39B
NGC 0741	20.9	36	0.071	0.16 ± 0.001	88.0 ± 1.1	0.14 ± 0.051	0.044 ± 0.021	N	E	5B
NGC 0777	21.4	1	0.0028	0.16 ± 0.001	148.6 ± 0.8	-0.25 ± 0.05	-0.26 ± 0.011		E	7B
NGC 0890	27.8	3	0.0079	0.39 ± 0.002	53.7 ± 0.3	-0.75 ± 0.05	-1.9 ± 0.02		E-S0	1
NGC 1016	16.3	10	0.0068	0.06 ± 0.001	42.8 ± 1.0	-0.14 ± 0.043	-0.17 ± 0.012		E	8B
NGC 1060	23.0	23	0.012	0.22 ± 0.001	74.8 ± 0.4	-0.094 ± 0.046	-0.46 ± 0.012		E-S0	12B
NGC 1129	20.9	81	0.043	0.17 ± 0.002	61.7 ± 0.9	-0.14 ± 0.028	-0.047 ± 0.026	NC	E	33B
NGC 1167	22.0	17	0.014	0.17 ± 0.002	71.2 ± 0.8	-1.1 ± 0.083	-0.17 ± 0.033		S0	3B
NGC 1272	20.0	87	0.0075	0.05 ± 0.002	1.2 ± 7.3	-0.076 ± 0.056	-0.14 ± 0.014		E	117
NGC 1453	27.4	11	0.0087	0.17 ± 0.001	30.1 ± 0.2	-0.32 ± 0.061	0.0084 ± 0.011		E	12B
NGC 1573	23.8	4	0.0046	0.29 ± 0.001	31.7 ± 0.1	0.41 ± 0.054	0.22 ± 0.011		E	15B
NGC 1600	24.3	5	0.0082	0.32 ± 0.001	8.8 ± 0.1	1.8 ± 0.095	-0.79 ± 0.015		E	16B
NGC 1684	24.4	10	0.041	0.29 ± 0.002	90.5 ± 0.7	1.5 ± 0.047	1.4 ± 0.059	DN	E	11B
NGC 1700	28.4	11	0.01	0.29 ± 0.001	90.6 ± 0.3	0.054 ± 0.051	0.95 ± 0.014		E	4B
NGC 2258	26.2	32	0.012	0.24 ± 0.001	150.8 ± 1.2	0.066 ± 0.056	-0.18 ± 0.045	N	S0	3B
NGC 2274	21.0	14	0.039	0.11 ± 0.001	165.0 ± 0.2	-0.42 ± 0.055	-0.15 ± 0.013		E	6B
NGC 2513	21.9	21	0.019	0.21 ± 0.001	168.8 ± 0.7	0.53 ± 0.038	0.03 ± 0.012	D	E	4B
NGC 2672	25.2	33	...	0.15 ± 0.002	136.8 ± 0.6	0.16 ± 0.042	-0.34 ± 0.023	N	E	3B
NGC 2693	20.8	64	0.018	0.27 ± 0.002	161.3 ± 1.3	-1 ± 0.028	-0.039 ± 0.015	DN	E	1
NGC 4914	20.8	1	0.014	0.39 ± 0.001	154.8 ± 0.1	1.6 ± 0.065	0.53 ± 0.016		E	1
NGC 5322	45.2	0	0.014	0.34 ± 0.001	92.1 ± 0.3	1.1 ± 0.046	-0.71 ± 0.016	D	E	8B
NGC 5353	37.6	26	0.039	0.50 ± 0.003	143.5 ± 0.8	-2 ± 0.047	-0.0085 ± 0.051	DN	S0	12B
NGC 5557	30.3	19	0.011	0.17 ± 0.001	90.5 ± 0.6	-0.13 ± 0.043	-0.41 ± 0.015		E	4B
NGC 6482	25.2	1	0.0078	0.22 ± 0.002	64.2 ± 0.5	-0.64 ± 0.048	1.1 ± 0.025		E	3B
NGC 7052	22.3	3	0.025	0.48 ± 0.001	63.4 ± 0.1	0.1 ± 0.018	-0.23 ± 0.013	D	E	1
NGC 7619	28.7	7	0.0045	0.23 ± 0.001	36.8 ± 0.2	1.2 ± 0.073	0.57 ± 0.013		E	12B

Note. — Column (1): galaxy name. Column (2): Scale of 7.5 kpc in arcsec on image. Column (3): Maximum change in PA over full radial range. Column (4): Luminosity-weighted central drift, defined as $\langle \Delta r \rangle_L = \langle \Delta r_{cen}/r_{geo} \rangle_L$ over the full radial range, where Δr_{cen} is defined in Section 3.2.3. Column (5): Luminosity-weighted ellipticity. Column (6): Luminosity-weighted PA. Column (7): Intensity-weighted $B_4 \times 100$. Column (8): Luminosity-weighted $B_4 \times 100$. Column (9): Features: D indicates dust in the center, N indicates presence of nearby neighbors, C indicates a double nucleus. Column (10): Morphological type from Hyperleada. Column (11): Number of group members in the 2MASS HDC group catalog (Crook et al. 2007); “B” indicates brightest group galaxy. Central drift values could not be measured for NGC 2672.

3.2.2. Isophotal Rotation

The degree of isophotal twisting (or change in PA) over the full radial regime is listed in Table 2. Separate isophotal twists were also calculated for the three radial regimes. Within a given radial region, the ΔPA was computed by taking the difference of the minimum and maximum value of the PA. The minimum and maximum values were computed by averaging the absolute minimum and maximum PA with the two adjacent isophotes. The isophotal twist is the difference between these characteristic minimum and maximum values in each radial regime. The sum of the PA twists in each radial regime sometimes overestimates the overall twist, so we also calculated the PA twist over the full radial range using the same method. Using the full radial range, 37% (13) of our galaxies feature a change in PA of more than $\sim 20^\circ$.

Two galaxies, NGC 1272 and NGC 2672, have significant isophotal twists beyond 7.5 kpc. NGC 2672 has a large nearby neighbor that distorts the measurement of its outer isophotes. The outer parts of NGC 1272 are very round (see Fig. 22), so the change in PA is probably insignificant.

Five galaxies in our sample (NGC 507, NGC 665, NGC 708, NGC 1129 and NGC 1272) have isophotal twists at radii between 0.75 and 7.5 kpc. NGC 665 is a barred S0 galaxy; its profile has discontinuities in the ellipticity and position angle at the boundaries between the inner spheroid and nuclear dust disk, the stellar bar, and the outer disk. The interior of NGC 708, the cD galaxy in Abell 262, is obscured by an extended, irregular dust structure stretching ~ 5 to 10 arcsec from the center, which creates a large and discontinuous twist of its isophotes. NGC 507 has an isophotal twist of 70° outside of ~ 10 arcsec without any sign of dust; Lauer et al. (2005) also observed a change in PA in the nucleus, inside 0.4 arcsec. It also has a bright nearby companion to the north, just outside the WFC3/IR field of view, which may explain the isophotal distortion. NGC 1129, which appears to be a merger remnant with a double-peaked nucleus (see Section 3.4), has isophotes that twist by almost 83° outside of 2 arcsec. This is consistent with Peletier et al. (1990), who found a rotation of 90° over the full radial range for NGC 1129. The very large twists in these galaxies suggest that they are either triaxial with

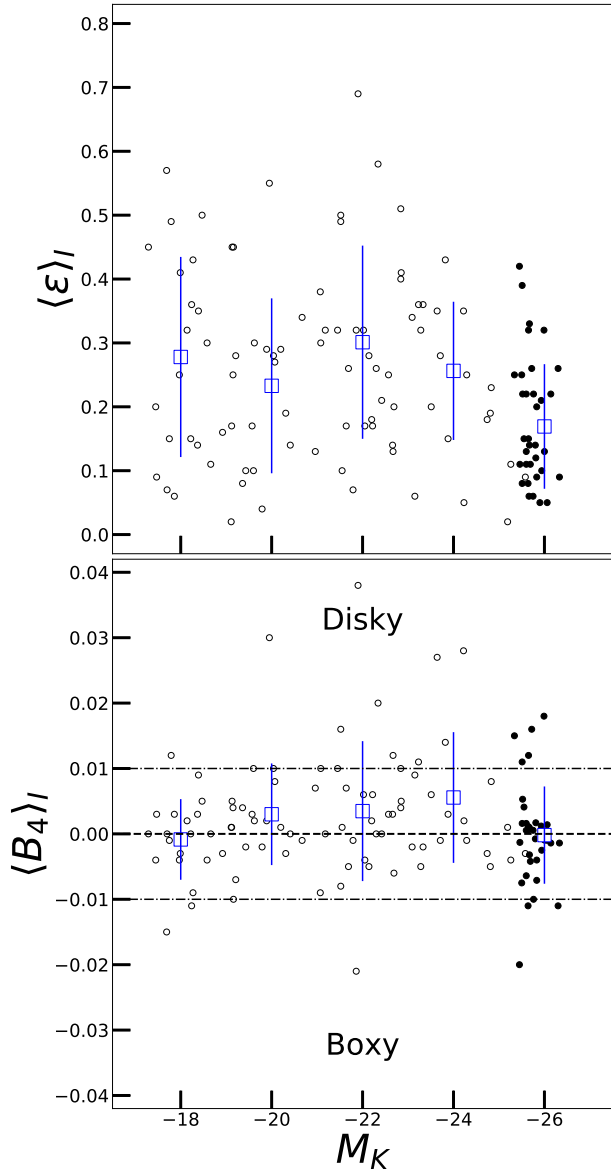


Figure 2. Intensity-weighted mean ellipticity and B_4 for each galaxy, plotted against K -band magnitude, which scales with mass. Only isophotes with semi-major axis $1'' < a < 7.5$ kpc were used. Open circles are values from the ACS Virgo Cluster Survey (Ferrarese et al. 2006). Filled circles are values for the MASSIVE galaxies presented in this paper. Blue open squares are the average values after sorting the combined samples into magnitude bins 2 mag wide. Error bars were generated from the scatter in each bin, and span a range of 2σ .

a favorable viewing orientation or they have disrupted isophotes, potentially due to a recent major merger or interaction.

Isophotal rotation measurements inside 0.75 kpc seen in two of our galaxies (NGC 665 and NGC 2258) are not significant due to the presence of nuclear dust and round isophotes, respectively.

There are a few cases that show a modest, systematic twist of less than 20° over their radial profiles. NGC 1060, NGC 1167, NGC 1453, NGC 1573, NGC 1600, and NGC 2513 all display consistent shifts in PA that do not have inflection points or discontinuities, possibly because they are triaxial, rather than because

of recent interactions with neighboring galaxies.

3.2.3. Isophotal Central Drift

In addition to looking for twisting isophotes, we have examined our sample for signs of drifting isophotal centers (Table 2). The drift $\Delta r_{cen} = \sqrt{\Delta a \Delta b}$ was calculated by taking the luminosity-weighted average of the shift in central position over each radial regime. The measured drift is relative to the center of the innermost isophote. A significant drift of the isophotal centers may indicate that the galaxy’s spheroidal component and central black hole do not lie at the bottom of the potential well created by the overall stellar mass distribution of the galaxy.

Most of the galaxies in our sample with significant central drift $\Delta r_{cen}/r_{geo} \geq 0.1$ outside of 0.4 arcsec are galaxies with dust in their centers, which obscures or distorts the true centers of the interior isophotes. Many galaxies feature potentially significant drifts deep in their interiors (within 0.4 arcsec), but these isophotes have been excluded from our analysis due to being within two times the FWHM of the PSF of the center. Three galaxies, NGC 741, NGC 665, and NGC 1129, have significant drifts in their outer isophotes that are not explained by the presence of dust. The central drift in NGC 741 occurs around 10 arcsec, and is likely due to multiple interactions the galaxy is undergoing with nearby neighbors. The central drift observed in NGC 665 accompanies the sudden change in ellipticity and B_4 that marks the transition between the stellar bar and outer disk. NGC 1129 shows multiple signs of a recent major merger. If the interaction is recent enough, the outermost stellar orbits may not necessarily have settled around the new center, which would explain the displacement of NGC 1129’s outermost isophotes.

3.2.4. Boxy and Disky Deviations from Elliptical Isophotes

We also measured the boxiness or diskiness as a function of radius, with luminosity and intensity-weighted mean values listed in Table 2. Figure 2 displays the intensity-weighted ellipticity and B_4 parameters as a function of the K -band magnitude, which is a proxy for mass, using data from our sample and from the ACSVCS sample (Ferrarese et al. 2006). The accepted paradigm for early type galaxies is that high mass galaxies commonly have boxy isophotes, while their lower mass counterparts typically have disk isophotes (Ferrarese et al. 1994; van den Bosch et al. 1994; Lauer et al. 1995; Rest et al. 2001; Lauer et al. 2005; Ferrarese et al. 2006), where the boxiness or diskiness of a galaxy is determined by whether the parameter B_4 is positive (disky) or negative (boxy). Whether the deviation is significant enough to call a galaxy boxy or disk is typically given by the condition that $|B_4 \times 100| \gtrsim 1$ (Jedrzejewski 1987).

Using an intensity-weighted mean, which gives a higher weighting to the inner isophotes, our sample contains five disk and four boxy galaxies, where the remaining 26 galaxies have B_4 values consistent with purely elliptical profiles. The average intensity-weighted B_4 for our sample is $B_4 = -0.00002 \pm 0.0077$, consistent with zero. If we use a luminosity-weighted mean, which gives heavier weighting to the outer isophotes (near a radius of 7.5 kpc), our sample contains five disk and two boxy galaxies and has a mean $B_4 = -0.00009 \pm 0.0063$, also

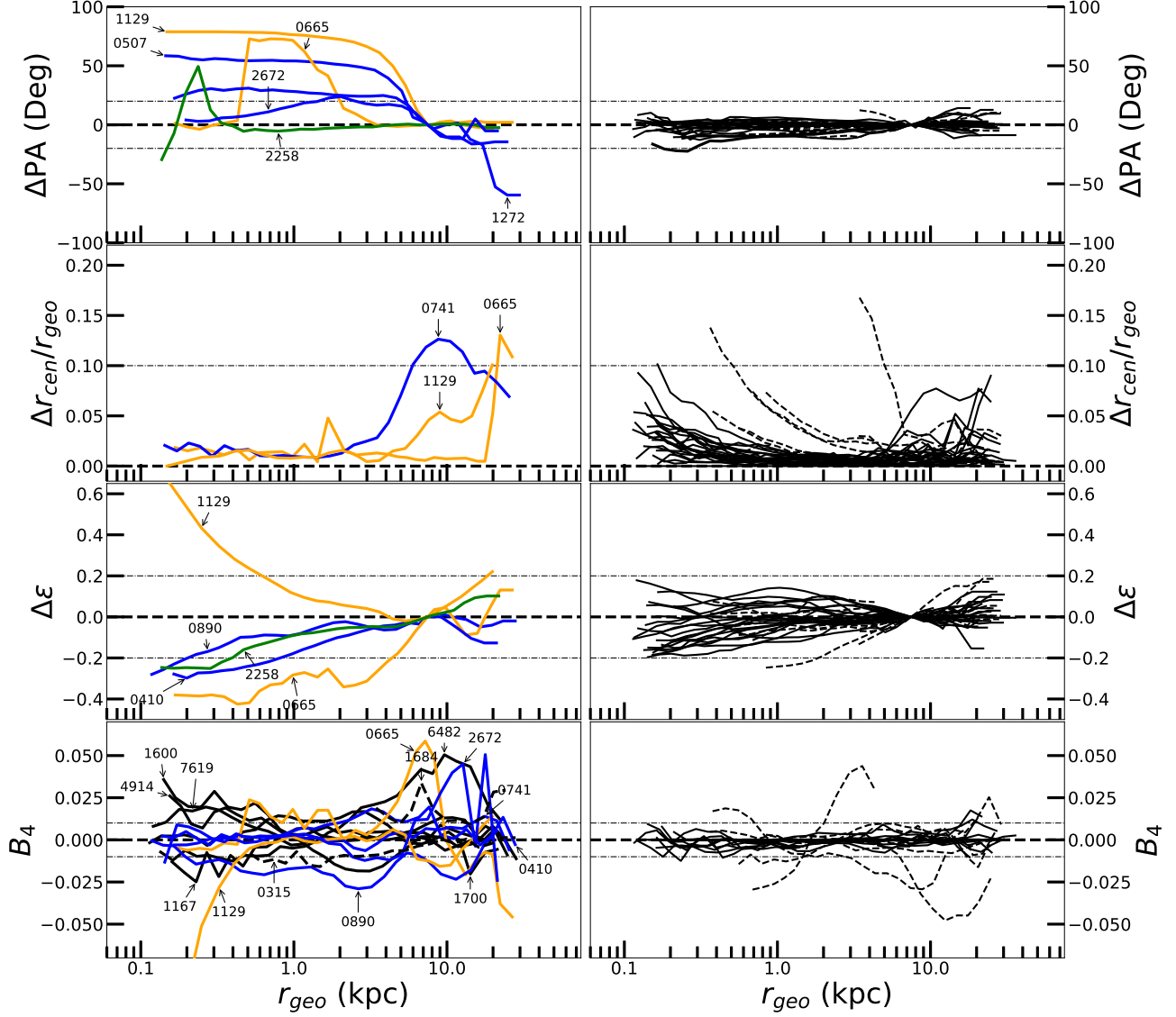


Figure 3. Parameter shifts as a function of geometric mean radius $r_{geo} = \sqrt{ab}$. The top panel shows the change in PA from the PA at a reference radius of 7.5 kpc. The second panel shows the central drift $\Delta r_{cen}/r_{geo}$. The third panel shows the change in ellipticity at the reference radius. The lower panel shows B_4 . The line colors in the left plots indicate the number of parameters that have significant shift over their radial range. Blue, green, and gold lines indicate that multiple isophotes have a significant shift in one, two, or three parameters, respectively (not including the shift in B_4). Black lines indicate galaxies that only have a significant shift in B_4 . The plots on the left display the profiles of the galaxies with a significant shift in the plotted parameter, while plots on the right show the profiles of the rest of the galaxies that do not have a significant shift. Dashed lines refer to dusty galaxies, which, for the most part, were not counted as having significant shifts due to the presence of central dust. The dot-dashed lines indicate the (arbitrary) limits used for deciding which galaxies to highlight in the left panels.

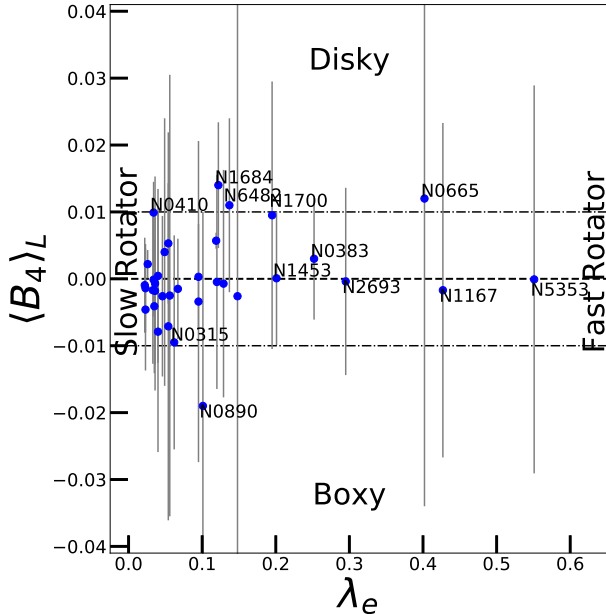


Figure 4. Plot of luminosity-weighted B_4 against the dimensionless spin parameter rotation criterion λ_e . Gray bars are not error bars; they indicate the full range of B_4 values found in a galaxy’s radial profile.

consistent with zero. For comparison, the high mass ($M_K < -24.5$) galaxies from the ACSVCS have a mean intensity weighted $B_4 = -0.001 \pm 0.0028$. Both our measures of mean B_4 are consistent with Ferrarese et al. (2006). We do see, however, that the mean B_4 not only shifts to slightly more negative values when outer isophotes are given heavier weighting, but the scatter also decreases compared to weighting schemes that prioritize the interior isophotes. Overall, our sample suggests that high mass early-type galaxies, while slightly boxy on average, often show a range of B_4 values, even within a single galaxy. Galaxies that appear to be significantly diskly or boxy with intensity weighting may not appear so when weighted by luminosity because of radial variations in B_4 . Galaxies with extreme mean B_4 values often exhibit the greatest variation in B_4 over their full radial profile. This can be seen in the bottom panels of Figure 3. The galaxies with boxy or diskly isophotes rarely maintain a consistent B_4 value over their full profile, and instead tend to have large variations in the value of B_4 . Only two galaxies in our sample, NGC 315 and NGC 890, have consistently boxy isophotes over their full radial profile, and only one galaxy, NGC 1684, has consistently diskly isophotes.

A second aspect of the typical early type galaxy paradigm is that fast rotators tend to be diskly, while slow rotators are preferentially boxy. In Figure 4, we examine the relationship between B_4 and rotation in our sample using the fast rotation criterion $\lambda_e > 0.2$ from Paper VII (Veale et al. 2017a) for comparison. The dimensionless parameter λ , the “spin parameter,” quantifies the rotation of a galaxy within the circularized radius r , and is given by

$$\lambda(< r) \equiv \frac{\langle r|V| \rangle}{\langle r\sqrt{V^2 + \sigma^2} \rangle}, \quad \lambda_e \equiv \lambda(< r_e), \quad (3)$$

where V is the stellar velocity and σ is the velocity dis-

persion. All averages are weighted by luminosity. The value of λ when the averages are calculated within the kinematically determined effective radius r_e is λ_e . The spin parameter criterion for identifying fast rotators is $\lambda_e > 0.2$ (Veale et al. 2017a; Lauer 2012). Figure 4 shows the luminosity-weighted average B_4 within 7.5 kpc plotted against λ_e . Of the six fast rotators in our sample, only one is significantly diskly; the others are consistent with purely elliptical profiles. One other galaxy, NGC 1700, which lies on the boundary between fast and slow rotators, is significantly diskly. The remaining 28 galaxies are slow rotators, and range from significantly boxy to significantly diskly. Most slow rotators have slightly negative B_4 values, where 19 have $B_4 < 0$ and the remaining nine have $B_4 > 0$. Overall, fast rotators have an average $B_4 = 0.0022 \pm 0.0046$, while slow rotators have an average $B_4 = -0.0007 \pm 0.0063$, consistent with zero. The slow rotators are purely elliptical on average, but individually they can range from significantly diskly to significantly boxy, with no clear preference for either extreme.

3.2.5. Connections Between Parameter Shifts

The radial variation in the isophotal parameters are shown for each galaxy individually in the Appendix. To look for trends in variations for the sample as a whole, we plotted the changes in PA, isophotal centers, ellipticity, and B_4 values together in Figure 3 as a function of radius. Because most galaxies only vary slightly, we separated those with significant variation from the rest for clarity. Galaxies with any significant isophotal shifts caused by dust were excluded. Of the remaining 26 galaxies, 9 have a significant shift in PA, center, or ellipticity. Two of these galaxies have shifts in at least two parameters. NGC 665 and NGC 1129 feature significant shifts in all three parameters. NGC 665 is a barred S0 galaxy with discontinuities at the boundaries between the stellar bar and the central regions and outer disk; NGC 1129 has a double-peaked nucleus indicating that it has probably experienced a recent merger. No obvious patterns emerge, and Figure 3 shows that the galaxies in this sample exhibit a rich variety of profiles, with individual galaxies having photometric structures that are highly individualistic and specific to their formation histories.

3.3. Dust Morphologies

Dust features are common in the interiors of early-type galaxies (Ferrarese et al. 2006; Lauer et al. 2005; Tran et al. 2001; Tomita et al. 2000). Of the 35 galaxies in our study, ten have clearly visible dust features in their centers (Table 2). Several previous studies found dust in about half of the early-type galaxies. Of the galaxies brighter than $B_T = 12.5$ mag in the sample of Ferrarese et al. (2006), 42% were found to have dust. Lauer et al. (2005) examined a heterogeneous sample of 77 archival *HST* images and found dust in 49% of their sample. Tran et al. (2001) examined a set of 68 early-type galaxies with radial velocities below 3400 km s^{-1} , absolute V -band magnitude less than -18.5 , and absolute galactic latitude above 20 degrees. Within this sample, 43% were found to have dust. Tomita et al. (2000) surveyed a set of 25 early-type galaxies in the *HST* archive imaged with WFPC2 in both V and I -band, and found dust in

56% of the galaxies. Ferrari et al. (1999) examined a sample of 22 early-type galaxies with $B_T > 13$ mag and found dust in 75% of their sample. van Dokkum & Franx (1995) looked at an archival *HST* sample of 64 early-type galaxies with *V*-band data and found a dust incidence rate of 48%. Our sample has a lower incidence of dust ($\sim 29\%$) than these other studies. Dust extinction in the near-IR is $\sim 15\%$ as large as at optical wavelengths, which could explain why this study finds dust less frequently than previous optical studies. Our lower dust incidence rate may also be due to the higher mass of this sample, as no previous studies have consistently probed galaxies with $M_* \gtrsim 10^{11.5} M_\odot$.

The dust features in our sample are most easily classified into three groups:

- G1: Irregular structures, such as wisps and lanes (NGC 708).
- G2: Medium to large, clumpy, irregular disks with typical radii of ~ 1.5 kpc (NGC 383, NGC 665, NGC 1684, NGC 5353).
- G3: Small, regular, smooth disks with typical radii of ~ 0.5 kpc (NGC 315, NGC 2513, NGC 2693, NGC 5322, NGC 7052).

It has been suggested that these groups form a dust settling sequence, where the dust is first pulled into the center, forming the structures in G1, then after a few orbits it settles into a more regular pattern as in G2, and after further orbital times the rings become smoother and more regular, finally settling into the structures seen in G3 (Tran et al. 2001). These small disks then feed the central black hole, thereby emptying from the inside out until the center is dust free. In this scenario, the irregularity of the first group would decay quickly into the more regular structures of the other two, thereby requiring a source for the dust seen in G1. Several authors have argued that an external source is required for this dust (Goudfrooij et al. 1994; van Dokkum & Franx 1995; de Koff et al. 2000; Tran et al. 2001). Ferrarese et al. (2006) suggest that the potential evolution of the dust from G1 to G2 to G3 means that even the regular, smooth dust rings require an external origin. Lauer et al. (2005) argued for a local origin from evolved stars.

We compared the occurrence of dust in our sample with the warm gas mass in Table 1 of Pandya et al. (2017), which has data for 12 of our 35 galaxies, of which four contain central dust. Our comparison shows that dusty and non-dusty galaxies have similar distributions of warm ionized gas mass. We also compared our sample to the molecular hydrogen mass in Table 2 of Davis et al. (2016), which contained four dusty and three non-dusty galaxies. Galaxies with dust in our sample have a higher molecular hydrogen mass than non-dusty galaxies by a factor of ~ 5 .

3.4. NGC 1129

The core of NGC 1129 has two nearly-identical peaks separated by ~ 1 arcsec. To determine if this was a double nucleus or a single nucleus bisected by a dust lane, we compared our F110W images with archival *HST* images taken by ACS in the F435W and F606W bands,⁶

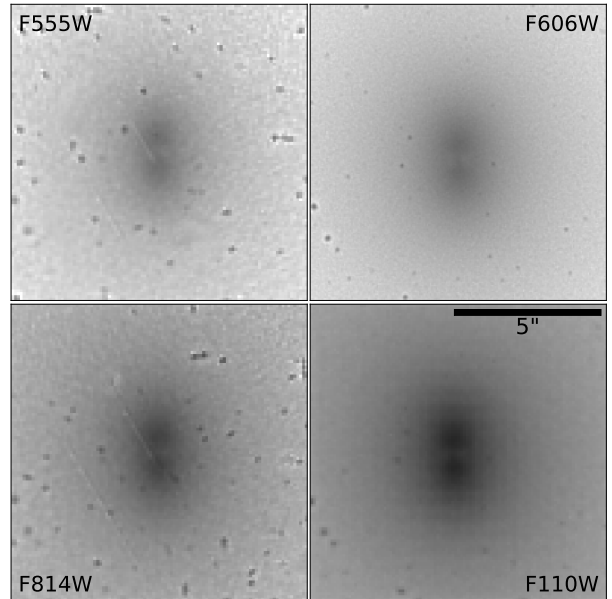


Figure 5. Images of the core of NGC 1129 in multiple wavelengths at the same spatial scale. The two peaks have close to the same brightness in all filters, and the dip in brightness between them does not become more or less pronounced in different wavelength filters. Images are shown with the same orientation and scaling, and have been sharpened to enhance the visibility of the two nuclei.

and by WFPC2 in the F555W and F814W bands.⁷ The images in Figure 5 show no evidence of differential extinction as a function of wavelength, leading us to conclude that NGC 1129 has two nearly-identical nuclei with no sign of dust. The presence of a double nucleus supports the case that NGC 1129 has recently undergone a major merger and the nuclei of the two galaxies have yet to coalesce. This would explain the extreme twisting in the outer isophotes and the inflection point in the ellipticity, which would naturally occur where the unmixed outer components of the progenitor galaxies no longer dominate the light profile. However, we cannot rule out the possibility that the core of NGC 1129 has a stellar torus seen edge-on (Lauer et al. 2002).

4. SUMMARY

Our photometric analysis of 35 of the most massive galaxies within 80 Mpc with $M_K < -25.5$ leads us to several interesting conclusions related to the evolutionary histories of these galaxies, and sets the stage for measuring the distances and black hole masses for these galaxies. In this study, we find that:

1. The ellipticities of the galaxies in our sample encompass a wide range of values, from a minimum intensity-weighted value of 0.08 to a maximum of 0.42. When combined with the ACSVCS sample, our results suggest that elliptical galaxies become rounder as their stellar mass increases (Fig. 2). Most galaxies in our sample are rounder within 7.5 kpc of the center than they are farther out (Fig. 3).
2. In our sample, we find that 37% (13) of the galaxies have isophotal rotations greater than 20° over

⁶ Program GO-13698, PI J. Lyman

⁷ Program GO-6810, PI D. Geisler

their full radial range (Table 2). Galaxies that are triaxial or that have recently been disrupted by mergers are likely to show significant rotations of their position angles. There is probably no single explanation for the twists; in some cases, the PA measurements are not meaningful because the isophotes are round. Excluding twists due to bars, dust, or neighbors, the three galaxies that display significant outer isophotal twisting (NGC 507, NGC 1129, and NGC 1272) appear to be the result of recent mergers.

3. Most of the galaxies in our sample do not have isophotes with center drifts greater than 10% of the semi-major axis length for that isophote (Fig. 3). Those that do are barred S0 galaxies, are interacting with neighbors, or have recently merged.
4. The average intensity-weighted boxiness of our sample is $B_4 = -0.00002 \pm 0.0077$ and is consistent with previous findings by Ferrarese et al. (2006), who found $B_4 \sim 0$ at the high mass end of their sample. The addition of our higher mass sample supports the conclusion of Ferrarese et al. (2006) that B_4 decreases towards zero from positive (diskier) values as stellar mass increases. When segregated by luminosity-weighted spin parameter (Fig. 4), we find that all the fast rotators are either significantly diskier ($B_4 > 0.01$), or have isophotes that are close to elliptical ($0.01 > B_4 \gtrsim 0$). Overall, fast rotators are slightly diskier on average, but with a luminosity-weighted average $B_4 = 0.0022 \pm 0.0046$ that is consistent with zero. Slow rotators are purely elliptical on average, with a luminosity-weighted average $B_4 = -0.0007 \pm 0.0063$ also consistent with zero. Slow rotators occupy a wide range of B_4 values, from approximately -0.02 to 0.015 , with most being clustered near $B_4 \sim 0$. There are roughly the same number of significantly diskier slow rotators as significantly boxy ones; in aggregate the slow rotators display a preference for elliptical isophotes. The lack of boxy galaxies among the fast rotators suggest that fast rotators are more likely to be diskier, but galaxies with a low spin parameter may or may not be boxy. Individual galaxies with significantly boxy or diskier B_4 values also show complex radial variations and a wide range in B_4 , making it difficult to interpret the measurement of any particular galaxy as being overall boxy or diskier (Fig. 3).
5. Central dust is slightly less prevalent ($\sim 29\%$) in our sample than in previous studies of early-type galaxies, which found roughly half of the galaxies contained central dust, but dust that would be visible in optical images may not be visible in our F110W IR images. Most of the central dust in our sample takes the form of dust disks, though smooth compact disks (G2) and irregular extended disks (G3) occur in roughly equal numbers.

Our high-resolution WFC3/IR images of 35 MASSIVE galaxies reveal a wide variety of behaviors in isophotal parameters. Some broad trends, such as diskiness and ellipticity decreasing at higher stellar masses, can be seen

in the data. These descriptions, however, belie the degree to which individual galaxies vary in these parameters over their full radial range. B_4 values vary substantially in massive elliptical galaxies and the galaxies with the most extreme B_4 values often exhibit the greatest variation in B_4 over their full radial profile. The breadth of isophotal parameter variations that we report in this paper suggests that more nuanced descriptions of the shapes of massive early-type galaxies should be used in galaxy formation studies, beyond simple classifications by a single parameter such as a global B_4 , PA, or ellipticity.

ACKNOWLEDGEMENTS

The authors thank John Lucey for his 2MASS profiles and Gabriel Brammer for his specialized Python program. C.F. Goullaud would like to thank Melanie Veale and Tom Zick for insightful discussions. The MASSIVE survey is supported in part by NSF AST-1411945, NSF AST-1411642, HST-GO-14219, and HST-AR-14573. This study was based on observations made with the NASA/ESA *Hubble Space Telescope*, obtained at the Space Telescope Science Institute, which is operated by the Association of Universities for Research in Astronomy, Inc., under NASA contract NAS 5-26555. These observations are associated with program GO-14219.

REFERENCES

- Bertin, E., & Arnouts, S. 1996, *A&AS*, 117, 393
- Brammer, G., Pirzkal, N., McCullough, P., & MacKenty, J. 2014, Time-varying Excess Earth-glow Backgrounds in the WFC3/IR Channel, Tech. rep.
- Cappellari, M., Emsellem, E., Krajnović, D., et al. 2011, *MNRAS*, 413, 813
- Carter, D. 1978, *MNRAS*, 182, 797
- Ciambur, B. C. 2015, *ApJ*, 810, 120
- Côté, P., Blakeslee, J. P., Ferrarese, L., et al. 2004, *ApJS*, 153, 223
- Côté, P., Ferrarese, L., Jordán, A., et al. 2007, *ApJ*, 671, 1456
- Crook, A. C., Huchra, J. P., Martimbeau, N., et al. 2007, *ApJ*, 655, 790
- Davis, T. A., Greene, J., Ma, C.-P., et al. 2016, *MNRAS*, 455, 214
- de Koff, S., Best, P., Baum, S. A., et al. 2000, *ApJS*, 129, 33
- Emsellem, E., Cappellari, M., Krajnović, D., et al. 2007, *MNRAS*, 379, 401
- . 2011, *MNRAS*, 414, 888
- Faber, S. M., Tremaine, S., Ajhar, E. A., et al. 1997, *AJ*, 114, 1771
- Ferrarese, L., van den Bosch, F. C., Ford, H. C., Jaffe, W., & O’Connell, R. W. 1994, *AJ*, 108, 1598
- Ferrarese, L., Côté, P., Jordán, A., et al. 2006, *ApJS*, 164, 334
- Ferrari, F., Pastoriza, M. G., Macchetto, F., & Caon, N. 1999, *A&AS*, 136, 269
- Fitzpatrick, E. L. 1999, *PASP*, 111, 63
- Franx, M., Illingworth, G., & Heckman, T. 1989, *ApJ*, 344, 613
- Gerhard, O. E., & Binney, J. J. 1996, *MNRAS*, 279, 993
- Glass, L., Ferrarese, L., Côté, P., et al. 2011, *ApJ*, 726, 31
- Goudfrooij, P., Hansen, L., Jorgensen, H. E., & Norgaard-Nielsen, H. U. 1994, *A&AS*, 105
- Goulding, A. D., Greene, J. E., Ma, C.-P., et al. 2016, *ApJ*, 826, 167
- Graham, A. W., Erwin, P., Trujillo, I., & Asensio Ramos, A. 2003, *AJ*, 125, 2951
- Greene, J. E., Janish, R., Ma, C.-P., et al. 2015, *ApJ*, 807, 11
- Jarrett, T. H., Chester, T., Cutri, R., et al. 2000, *AJ*, 119, 2498
- Jedrzejewski, R. I. 1987, *MNRAS*, 226, 747
- Jensen, J. B., Blakeslee, J. P., Gibson, Z., et al. 2015, *ApJ*, 808, 91
- Jordán, A., Blakeslee, J. P., Peng, E. W., et al. 2004, *ApJS*, 154, 509
- Kormendy, J., & Bender, R. 1996, *ApJ*, 464, L119

- Kormendy, J., Fisher, D. B., Cornell, M. E., & Bender, R. 2009, ApJS, 182, 216
- Laine, S., van der Marel, R. P., Lauer, T. R., et al. 2003, AJ, 125, 478
- Lauer, T. R. 2012, ApJ, 759, 64
- Lauer, T. R., Ajhar, E. A., Byun, Y.-I., et al. 1995, AJ, 110, 2622
- Lauer, T. R., Gebhardt, K., Richstone, D., et al. 2002, AJ, 124, 1975
- Lauer, T. R., Faber, S. M., Gebhardt, K., et al. 2005, AJ, 129, 2138
- Lauer, T. R., Gebhardt, K., Faber, S. M., et al. 2007, ApJ, 664, 226
- Ma, C.-P., Greene, J. E., McConnell, N., et al. 2014, ApJ, 795, 158
- Magorrian, J. 1999, MNRAS, 302, 530
- Pandya, V., Greene, J. E., Ma, C.-P., et al. 2017, ApJ, 837, 40
- Peletier, R. F., Davies, R. L., Illingworth, G. D., Davis, L. E., & Cawson, M. 1990, AJ, 100, 1091
- Pirzkal, N. 2014, WFC3 ISR
- Renzini, A. 2006, ARA&A, 44, 141
- Rest, A., van den Bosch, F. C., Jaffe, W., et al. 2001, AJ, 121, 2431
- Rusli, S. P., Erwin, P., Saglia, R. P., et al. 2013, AJ, 146, 160
- Schlafly, E. F., & Finkbeiner, D. P. 2011, ApJ, 737, 103
- Sérsic, J. L. 1968, Atlas de Galaxias Australes (Cordoba, Argentina: Observatorio Astronomico)
- Stark, A. A. 1977, ApJ, 213, 368
- Statler, T. S. 1994, ApJ, 425, 458
- Theureau, G., Hanski, M. O., Coudreau, N., Hallet, N., & Martin, J.-M. 2007, A&A, 465, 71
- Thomas, J., Ma, C.-P., McConnell, N. J., et al. 2016, Nature, 532, 340
- Thomas, J., Saglia, R. P., Bender, R., et al. 2004, MNRAS, 353, 391
- Tomita, A., Aoki, K., Watanabe, M., Takata, T., & Ichikawa, S.-i. 2000, AJ, 120, 123
- Tonry, J. L., Blakeslee, J. P., Ajhar, E. A., & Dressler, A. 1997, ApJ, 475, 399
- Tran, H. D., Tsvetanov, Z., Ford, H. C., et al. 2001, AJ, 121, 2928
- Tremblay, B., & Merritt, D. 1996, AJ, 111, 2243
- Trujillo, I., Erwin, P., Asensio Ramos, A., & Graham, A. W. 2004, AJ, 127, 1917
- van den Bosch, F. C., Ferrarese, L., Jaffe, W., Ford, H. C., & O’Connell, R. W. 1994, AJ, 108, 1579
- van Dokkum, P. G., & Franx, M. 1995, AJ, 110, 2027
- Veale, M., Ma, C.-P., Greene, J. E., et al. 2017a, MNRAS, 471, 1428
- . 2018, MNRAS, 473, 5446
- Veale, M., Ma, C.-P., Thomas, J., et al. 2017b, MNRAS, 464, 356
- Vincent, R. A., & Ryden, B. S. 2005, ApJ, 623, 137
- Weijmans, A.-M., de Zeeuw, P. T., Emsellem, E., et al. 2014, MNRAS, 444, 3340
- Williams, T. B., & Schwarzschild, M. 1979, ApJ, 227, 56
- Willick, J. A., Courteau, S., Faber, S. M., et al. 1997, ApJS, 109, 333

APPENDIX

WFC3/IR IMAGES AND RADIAL PHOTOMETRIC PARAMETER PROFILES

Images and radial plots for the full sample are shown below (except for NGC 57, which is shown as Figure 1). The images in the right panels are: (*Upper Left*) the F110W band image, (*Lower Left*) the isophotes derived from the surface brightness profile model (semi-major axis increases by 15% between isophotes), (*Upper Right*) a closer view of the center of the F110W image (scaled to make central features, such as dust, more visible), and (*Lower Right*) the residual image with galaxy models subtracted. The radial plots in the left panels show the isophotal parameters as a function of the geometric mean radius, $r_{geo} = \sqrt{ab}$, where a is the semi-major axis and b is the semi-minor axis. The horizontal black dotted line in the surface brightness profile shows the background measurement. Open symbols denote isophotes that are affected by dust.

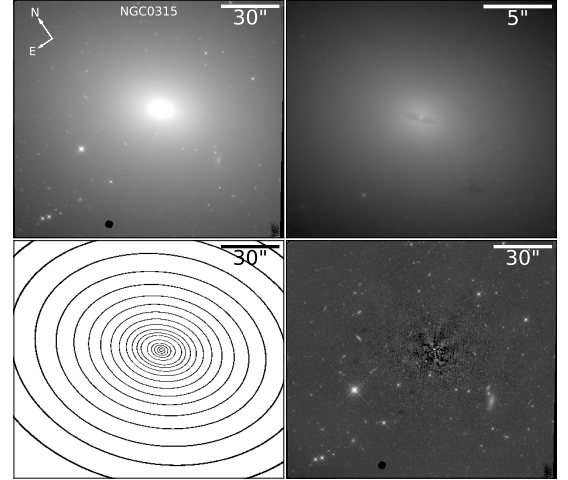
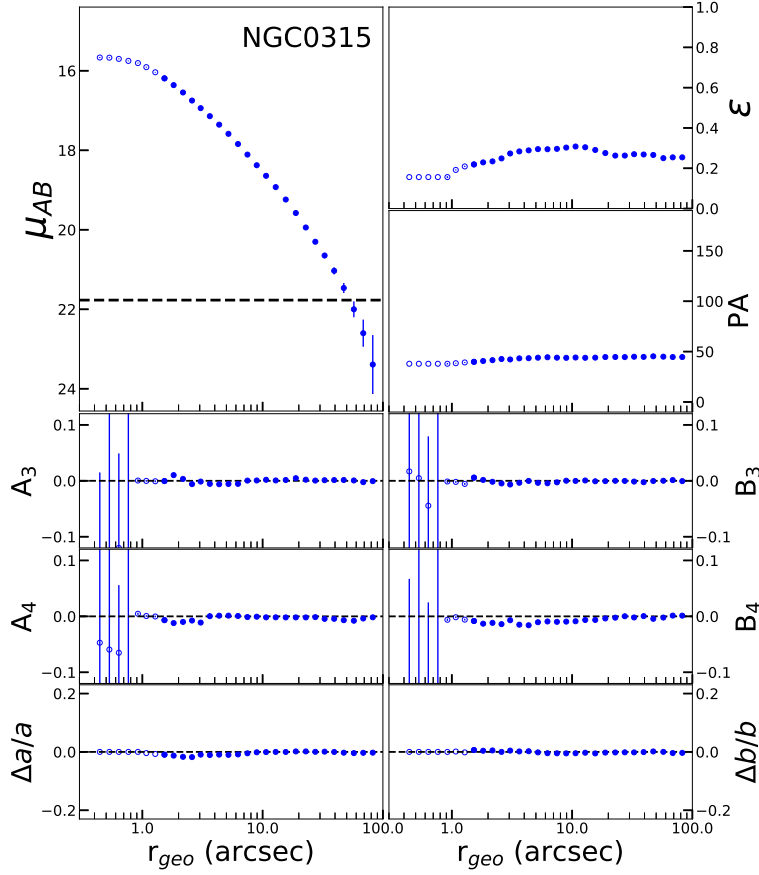


Figure 6. NGC 315 contains a small (~ 1.5 arcsec radius) compact nuclear dust disk that obscures the interior isophotes. The isophotes between ~ 1 – 10 arcsec show significant boxiness. This boxy region corresponds with an ellipticity that increases with radius. Outside ~ 10 arcsec, B_4 returns to zero and the ellipticity decreases with increasing radius. Scale: 1 arcsec = 341 pc.

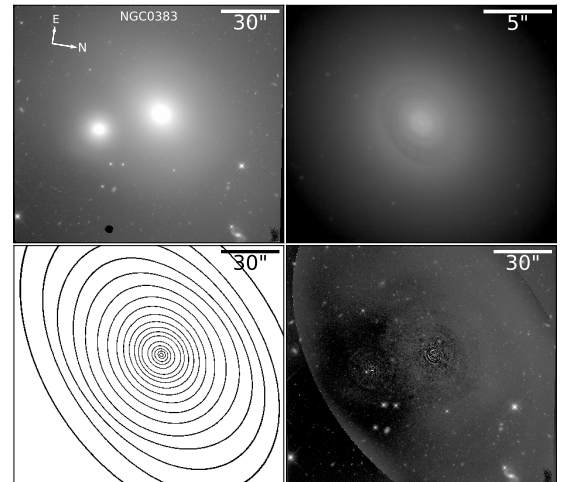
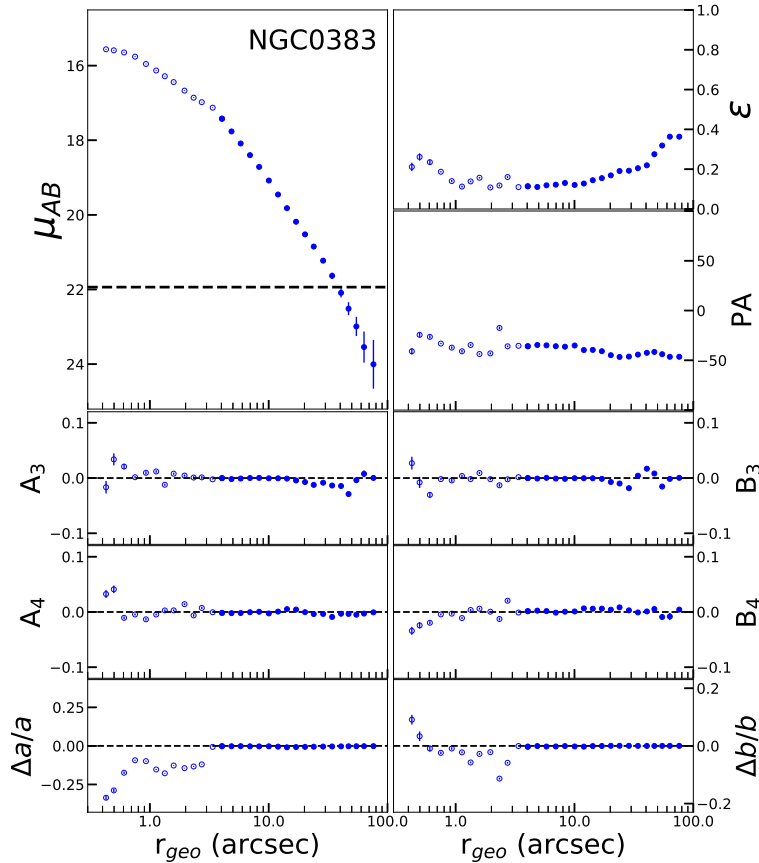


Figure 7. NGC 383 contains a ~ 4 arcsec radius nuclear dust disk, which obscures isophotes within that radius. The outermost isophotes, beyond ~ 40 – 50 arcsec, have an ellipticity that increases sharply with increasing radius. Inside that radius the ellipticity increases with radius. NGC 383 has a large nearby neighbor located 33 arcsec southwest of the center of NGC 383. Scale: 1 arcsec = 346 pc.

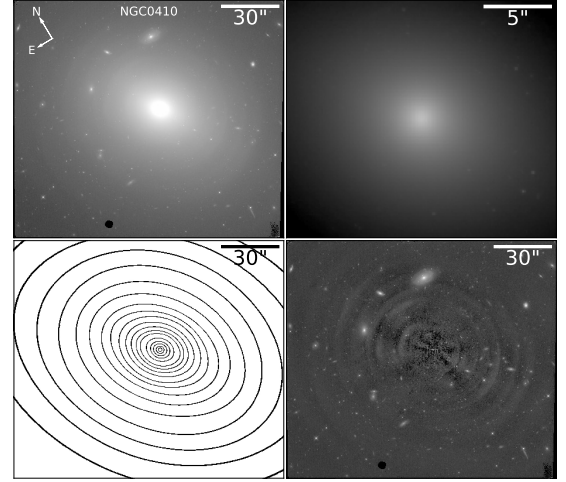
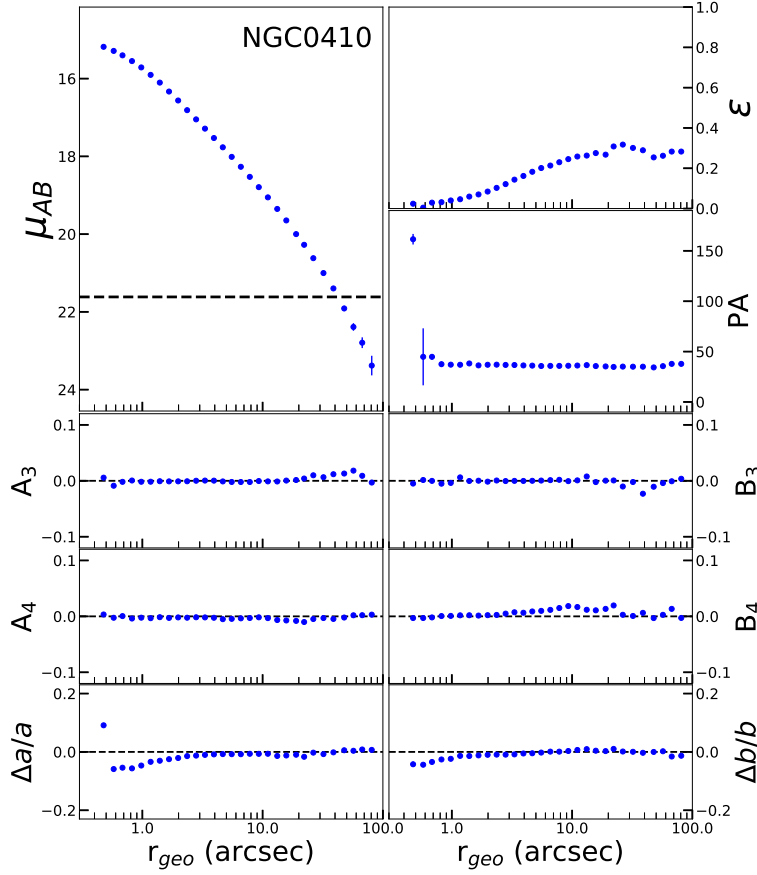


Figure 8. NGC 410 has disk isophotes between ~ 10 – 30 arcsec. Outside of this range the isophotes go back to $B_4 \approx 0$. The ellipticity also peaks at ~ 30 arcsec, beyond which it is approximately constant. Scale: 1 arcsec = 346 pc.

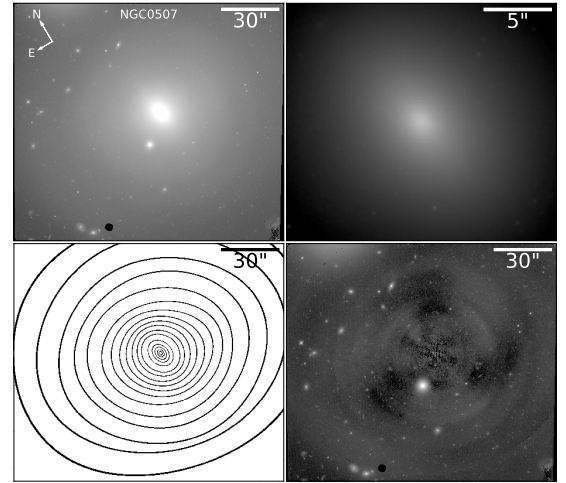
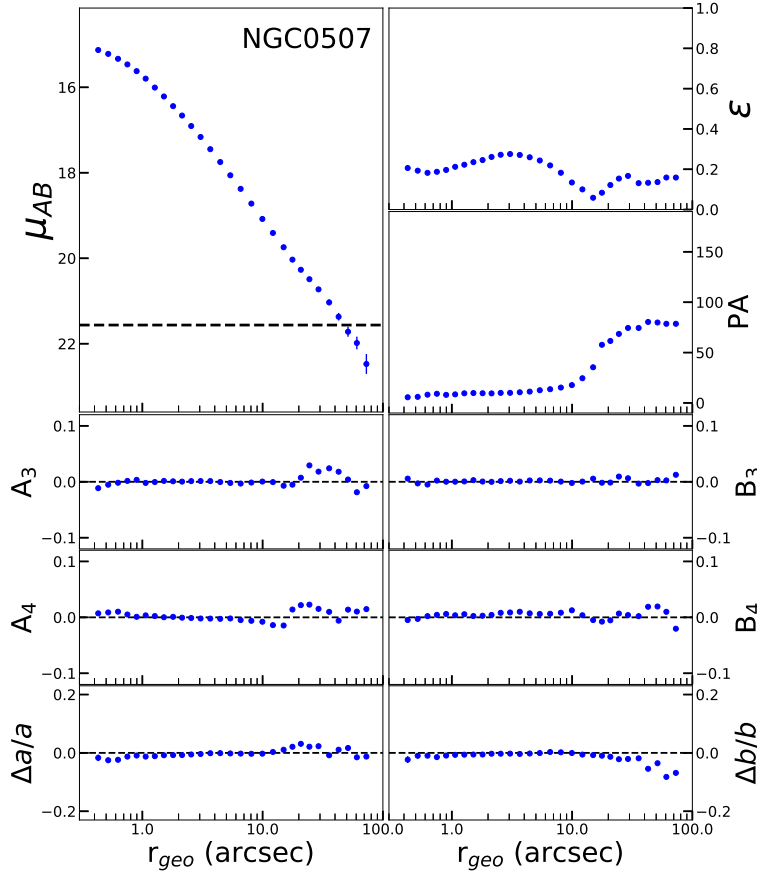


Figure 9. NGC 507 has one of the most dramatic PA twists in our sample. The PA changes by 71° between ~ 5 – 40 arcsec. The ellipticity also varies significantly, increasing up to its peak at ~ 2 arcsec before becoming nearly circular at ~ 15 arcsec (also the radius at which the PA twist is steepest), and finally rising to a moderate value for the outer isophotes. The isophotes between ~ 3 – 15 arcsec are disk, and isophotes beyond that radius have variable B_4 values. NGC 507 has an off-frame companion due North. Scale: 1 arcsec = 338 pc.

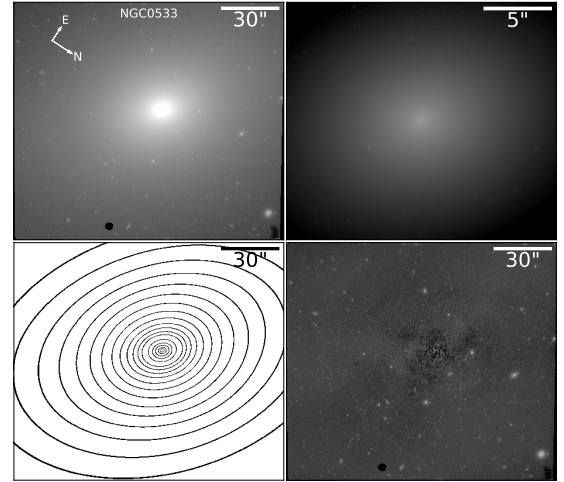
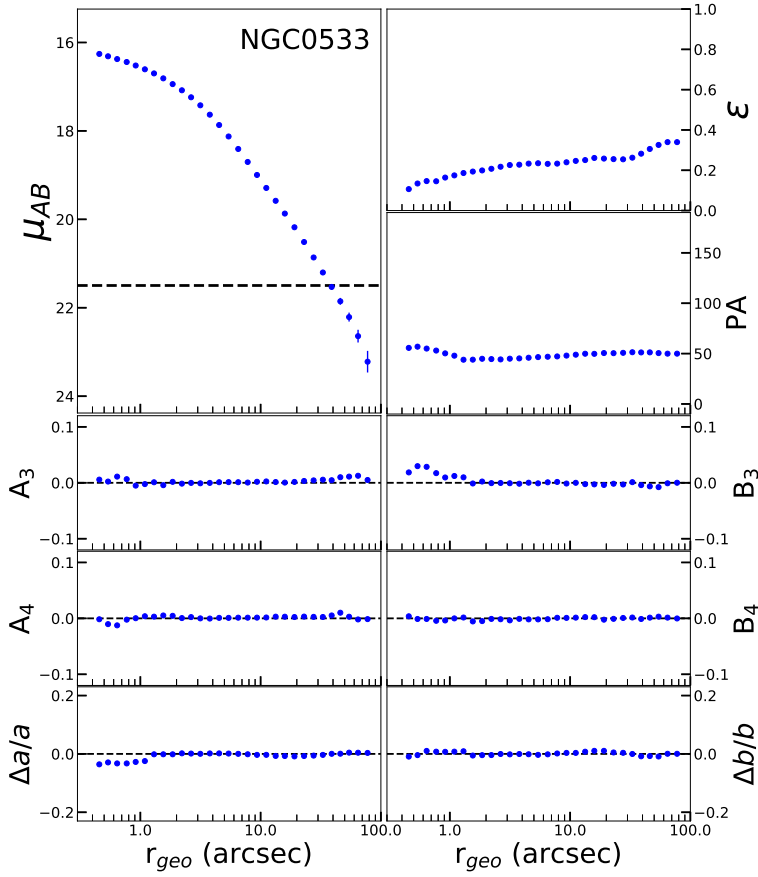


Figure 10. NGC 533 has ellipticity that increases with radius; the other parameters are nearly constant. Scale: 1 arcsec = 378 pc.

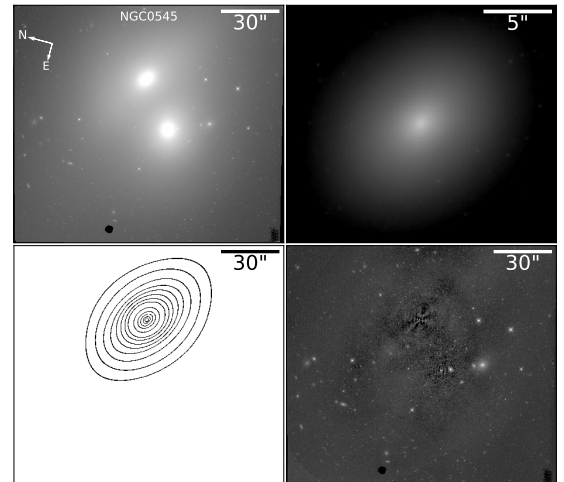
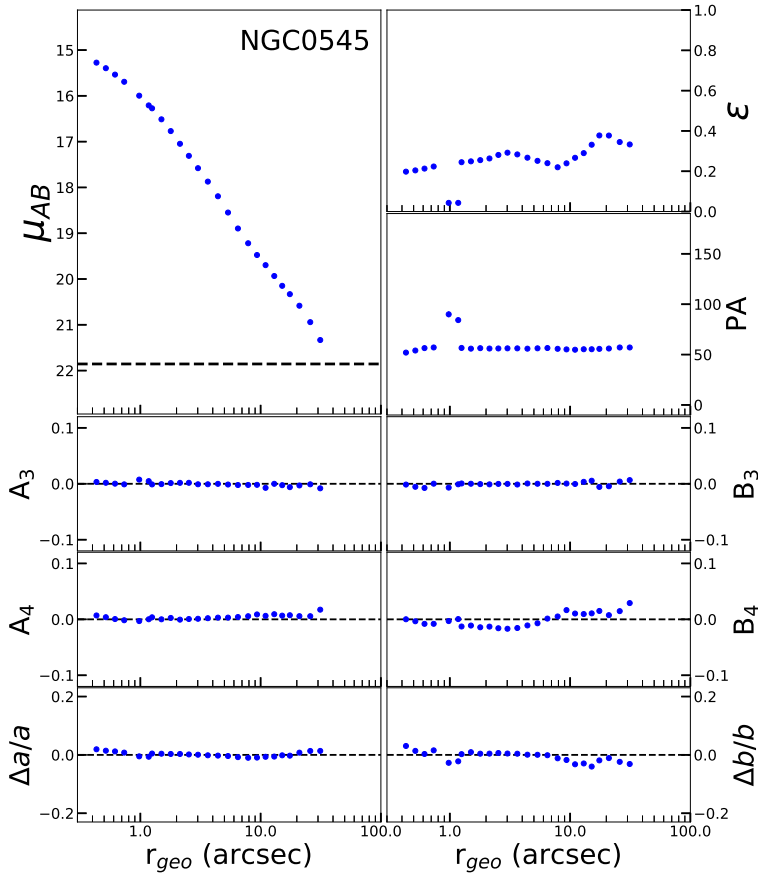


Figure 11. NGC 545 (the northern galaxy of the pair) has significantly disk-like isophotes beyond ~ 10 arcsec. Within this radius, the isophotes are significantly boxy. The beginning of this transition occurs at a local minima in ellipticity. It is difficult to separate the isophotes of the two galaxies beyond ~ 40 arcsec, so those isophotes have been removed from our analysis. NGC 545 has two isophotes at ~ 1 arcsec where ELLIPSE failed to generate good fits. Scale: 1 arcsec = 358 pc.

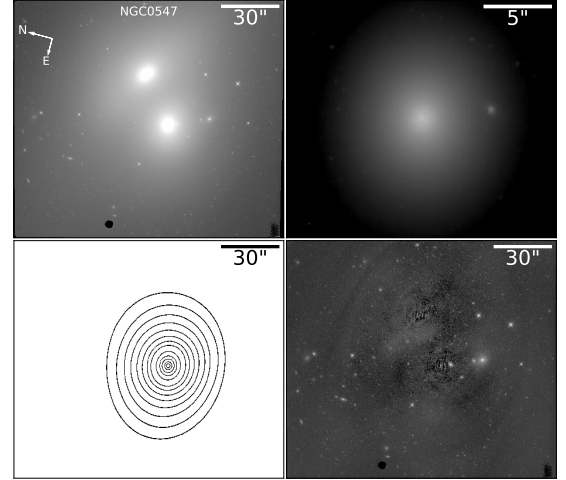
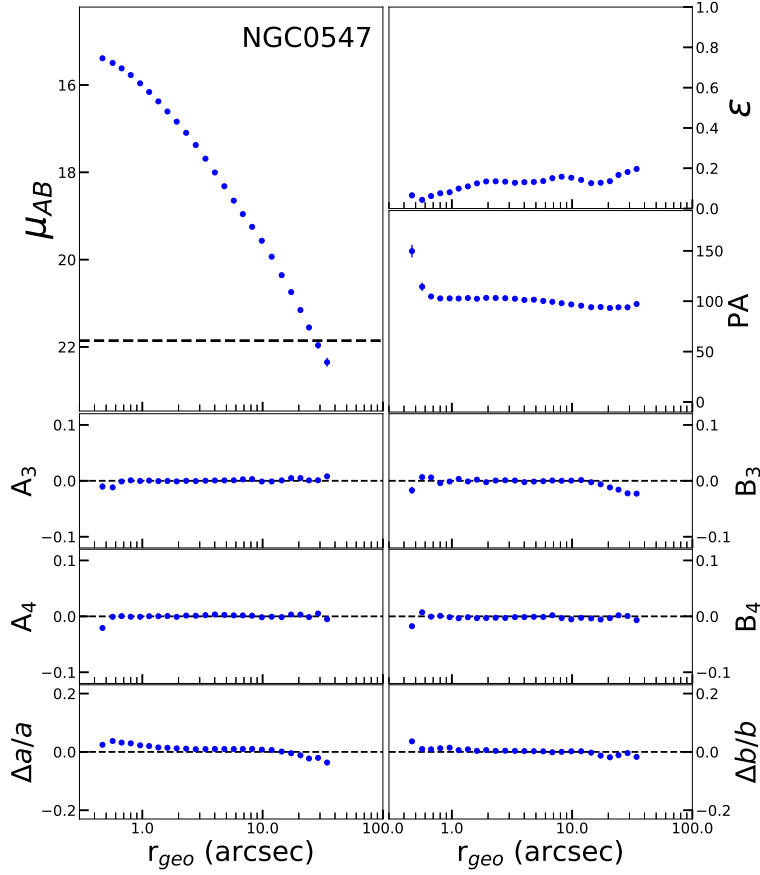


Figure 12. NGC 547 (the southern galaxy) has the beginnings of a PA twist within ~ 0.8 arcsec, though the degree of the twist is obscured by the PSF. It is difficult to separate the isophotes of the two galaxies beyond ~ 40 arcsec, so those isophotes have been removed from our analysis. Scale: 1 arcsec = 358 pc.

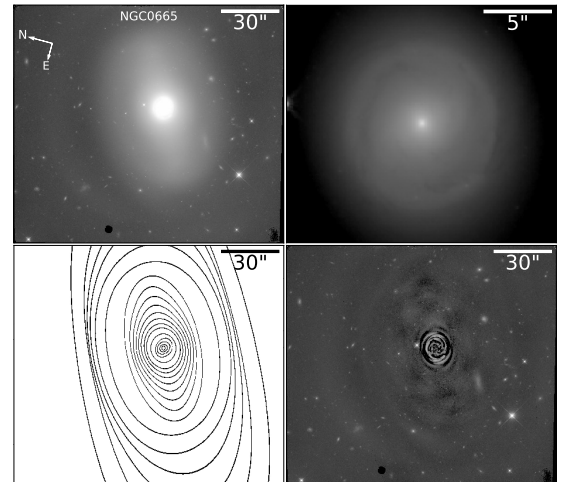
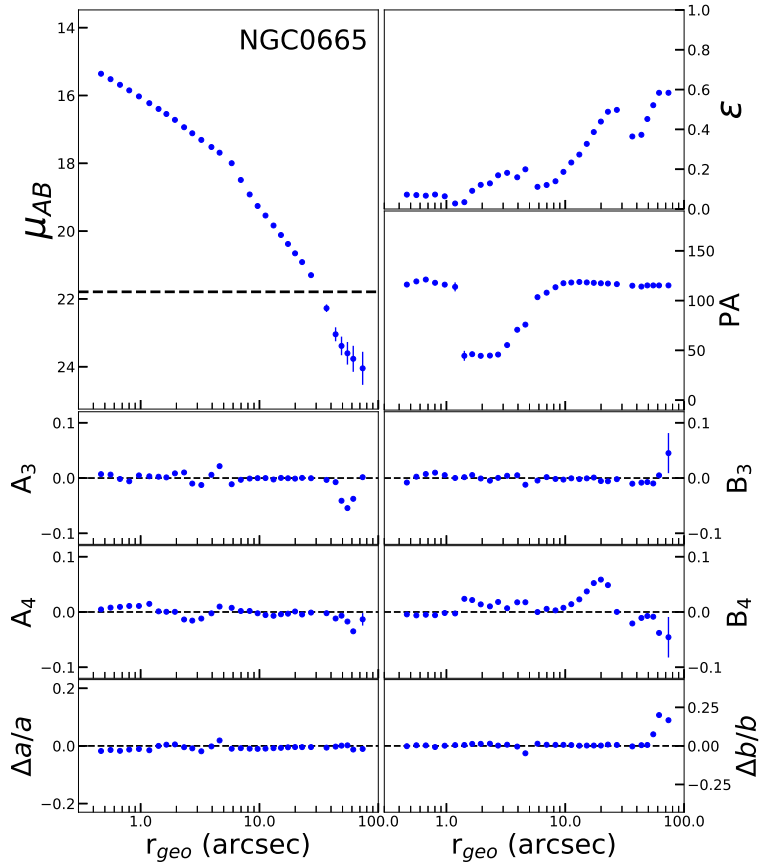


Figure 13. NGC 665 is a barred S0 galaxy with a bright nuclear peak and a dust disk which extends to a radius of ~ 4.5 arcsec. The stellar bar extends out to ~ 40 arcsec. The bright nucleus inside ~ 1 arcsec has a stable ellipticity and PA. The nuclear dust disk has a rising ellipticity and fairly stable PA. The PA rotates by 74° as the dust disk transitions to the stellar bar, and the ellipticity continues to rise. The outermost isophotes are very boxy and have displaced centers. Scale: 1 arcsec = 362 pc.

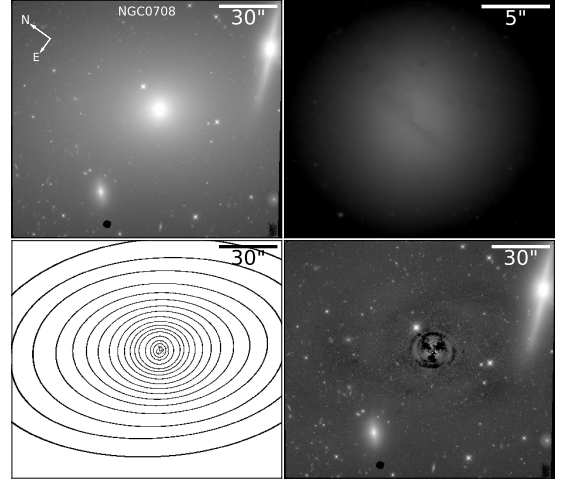
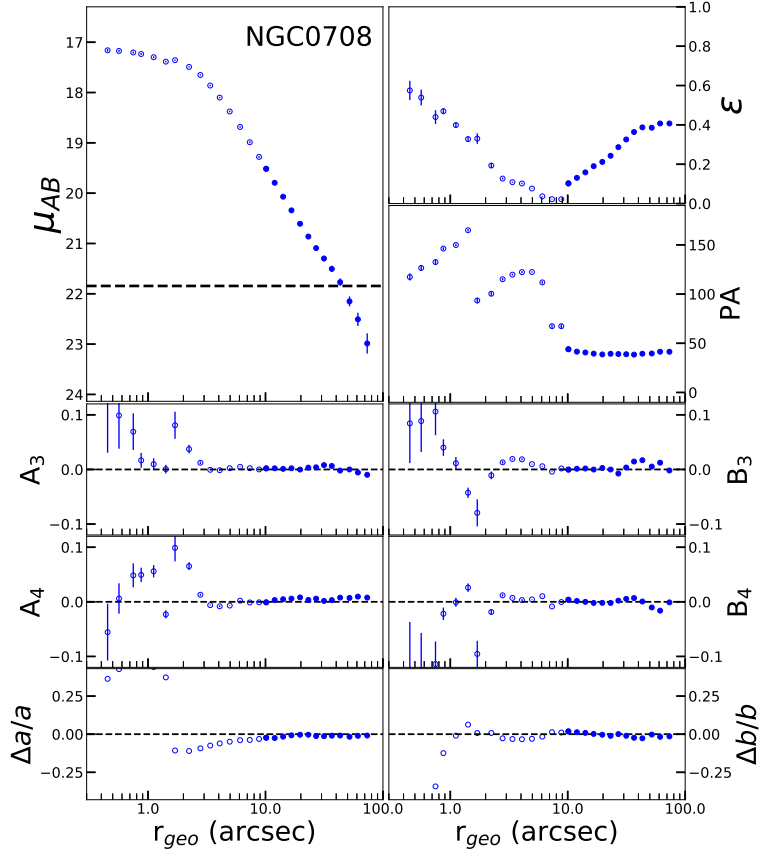


Figure 14. NGC 708 (the cD galaxy in Abell 262) has a large irregular dust structure, including a dust lane across the center, that obscures the central ~ 9 arcsec. NGC 708 has two smaller companions in the frame. Scale: 1 arcsec = 335 pc.

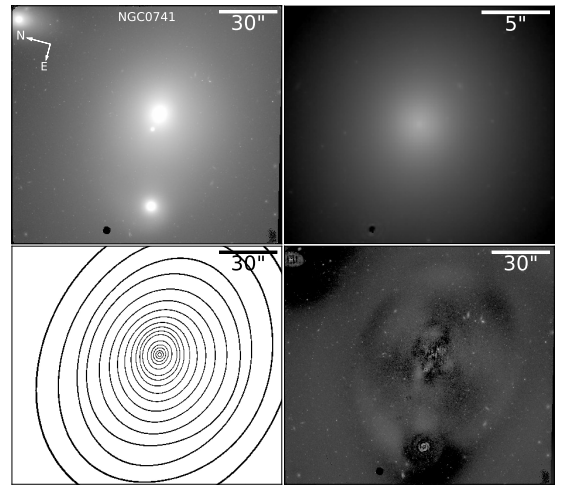
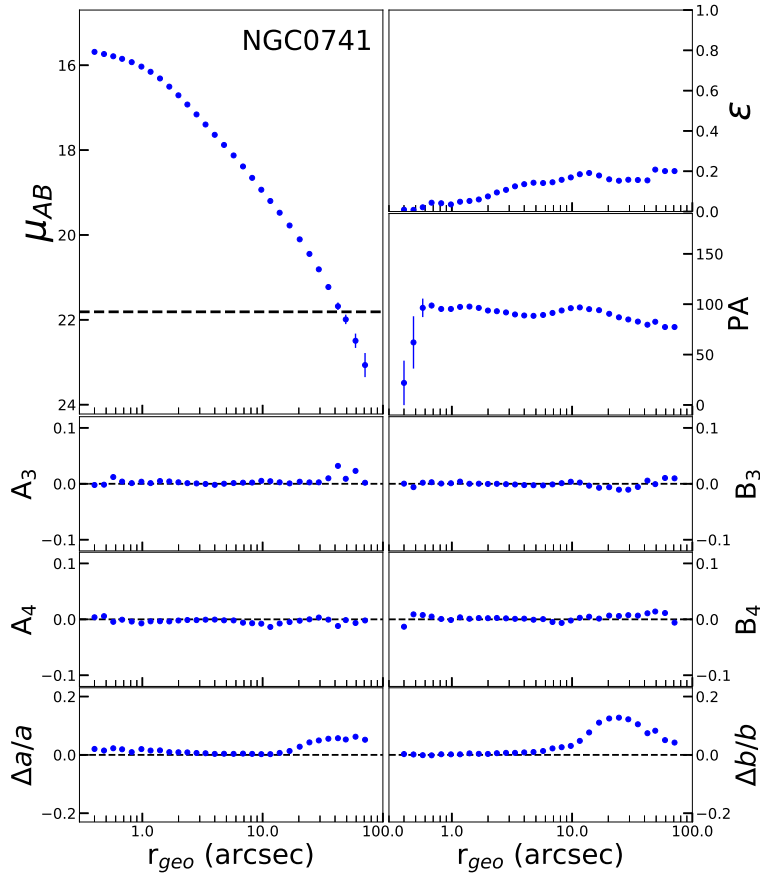


Figure 15. NGC 741 has a significant central drift to the south for isophotes starting at ~ 30 arcsec. It has three smaller companions in the frame. Two are east of the center, and one is north. Scale: 1 arcsec = 358 pc.

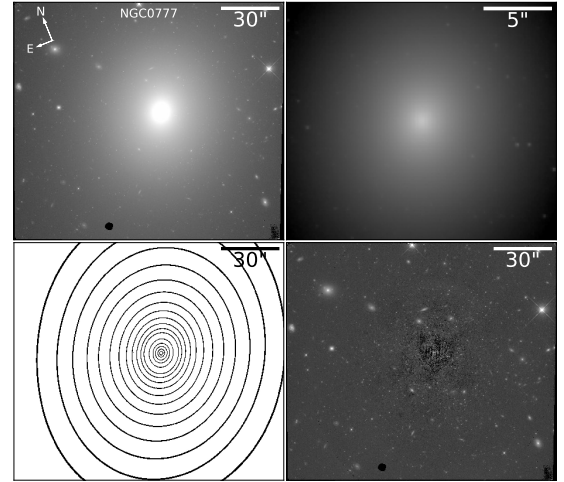
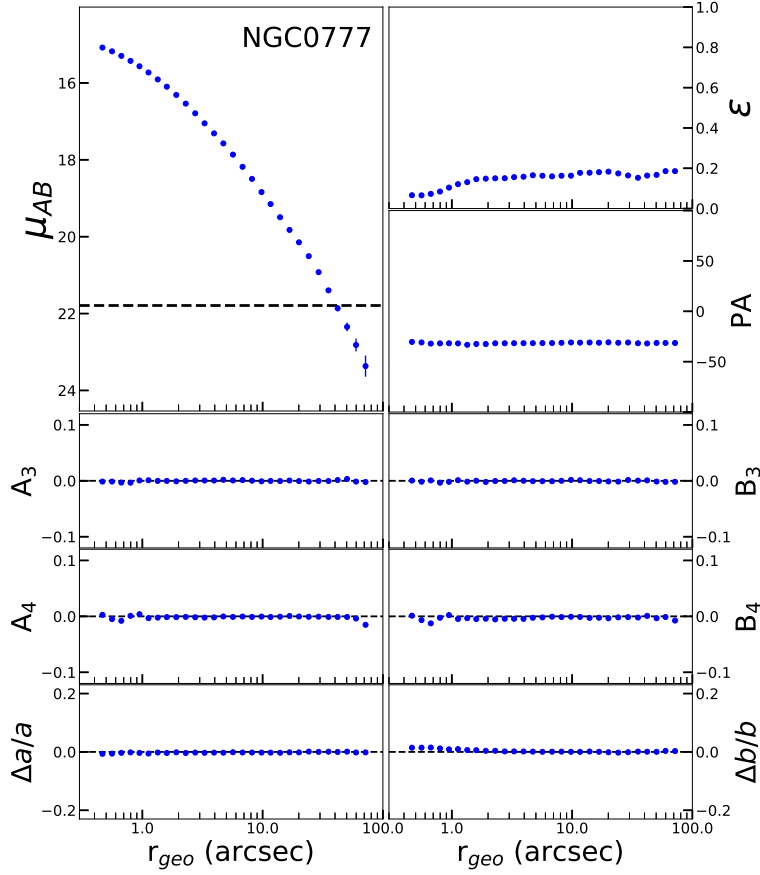


Figure 16. NGC 777 has slightly increasing ellipticity with radius; the other parameters are all nearly constant. Scale: 1 arcsec = 350 pc.

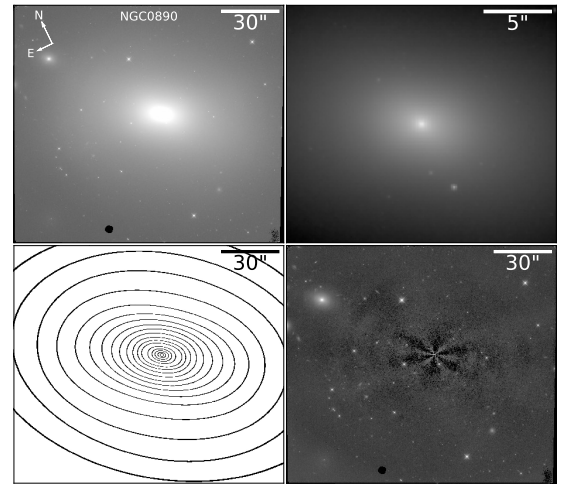
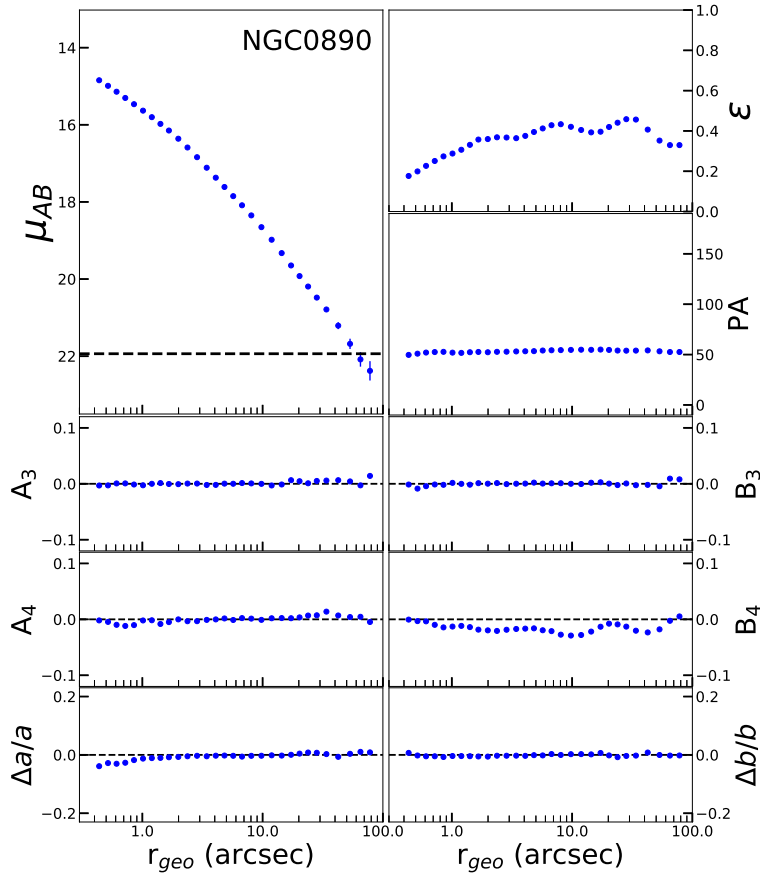


Figure 17. NGC 890 has a varying ellipticity that rises out to ~ 35 arcsec. The isophotes are boxy, but they become more elliptical outside ~ 35 arcsec. Scale: 1 arcsec = 270 pc.

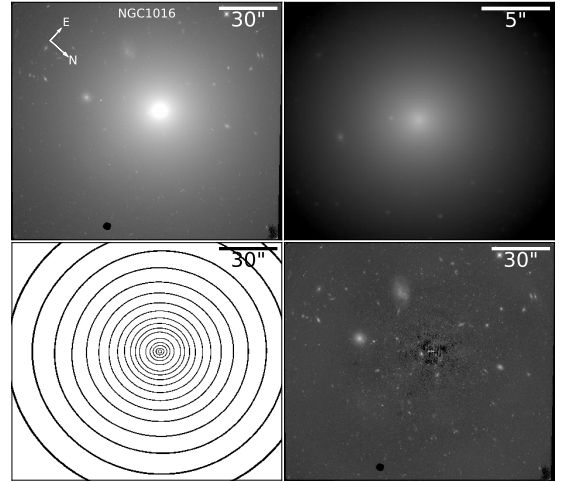
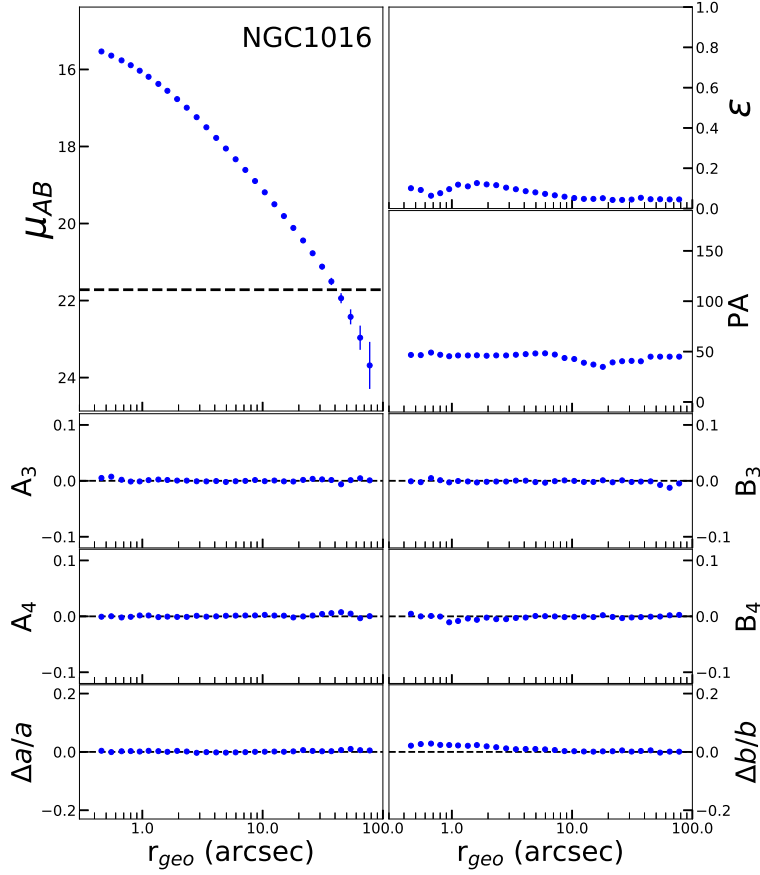


Figure 18. NGC 1016 is very round with nearly constant parameters. Scale: 1 arcsec = 462 pc.

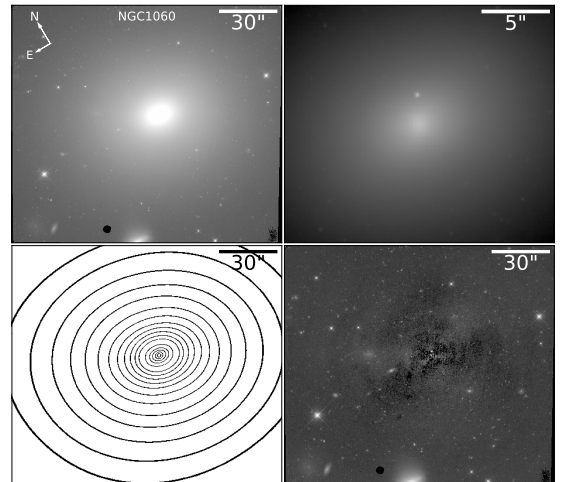
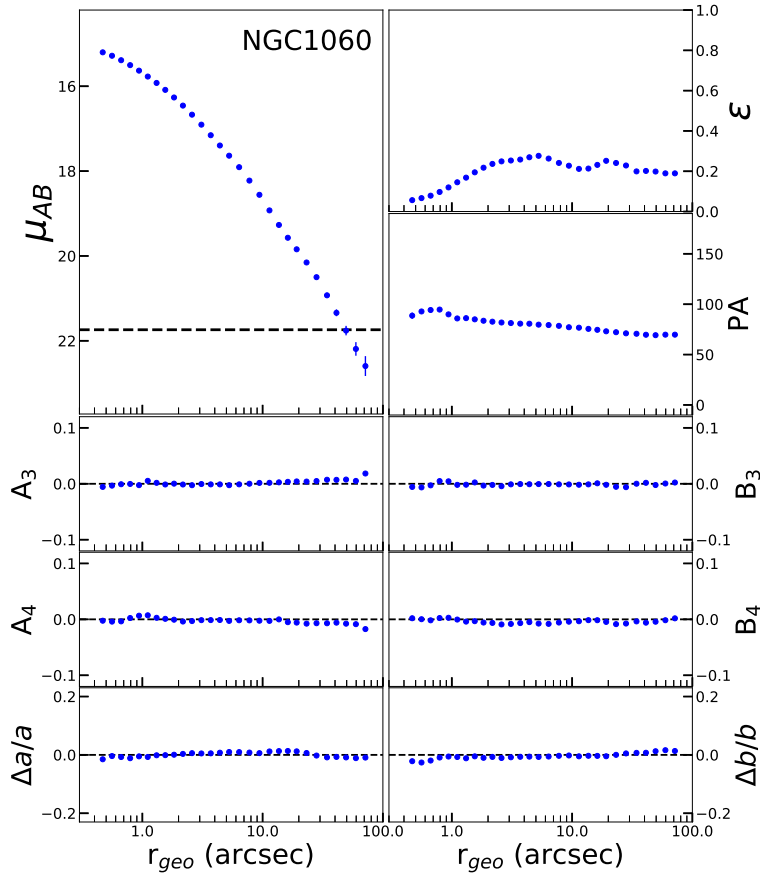


Figure 19. NGC 1060 has an ellipticity profile that rises as the radius increases, peaks at ~ 5 arcsec, and then undergoes a gradual decrease for isophotes beyond that radius. NGC 1060 has a small companion to the southeast. Scale: 1 arcsec = 327 pc.

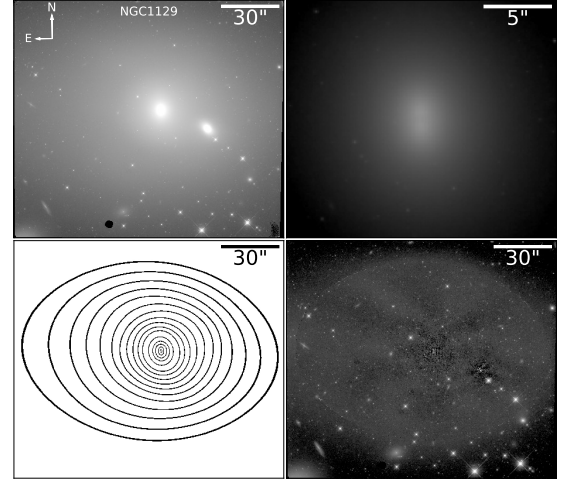
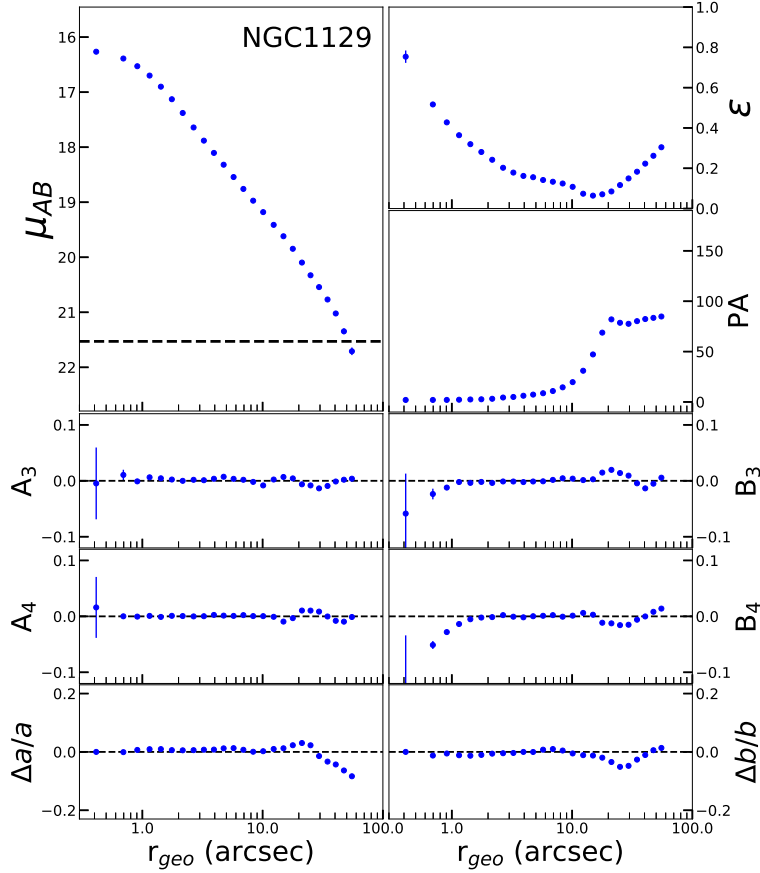


Figure 20. NGC 1129 has arguably the most interesting isophotes in our sample. The behavior of each parameter is split into two regimes. The inner regime extends to ~ 15 arcsec, and the outer regime extends beyond that. The inner region has a steeply decreasing ellipticity and increasing PA out to ~ 15 arcsec. These isophotes are neither boxy nor disk. The behavior of the isophotes abruptly changes in the outer region. The ellipticity begins increasing, the PA stabilizes, and the isophotes immediately become boxy, before becoming more disk for the outermost four isophotes. NGC 1129 has a double-peaked nucleus, suggesting it has undergone a recent merger. NGC 1129 has a small nearby companion 25 arcsec southwest from the center. Scale: 1 arcsec = 358 pc.

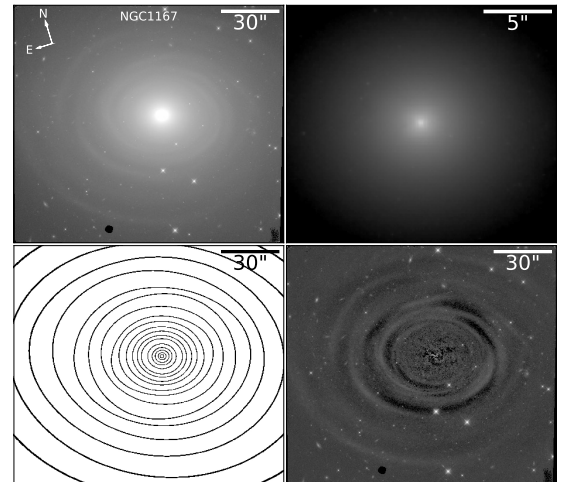
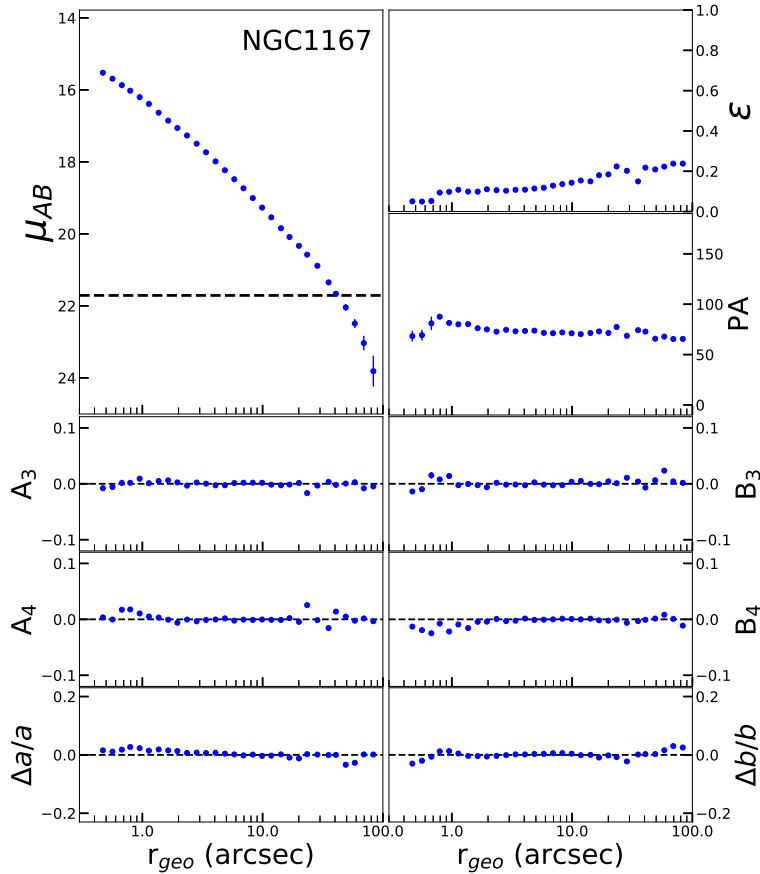


Figure 21. NGC 1167 is a S0 disk galaxy. Unlike NGC 0665, which has a strong bar, the NGC 1167 isophotes do not exhibit any special behavior beyond some boxiness within ~ 1.5 arcsec. Scale: 1 arcsec = 340 pc.

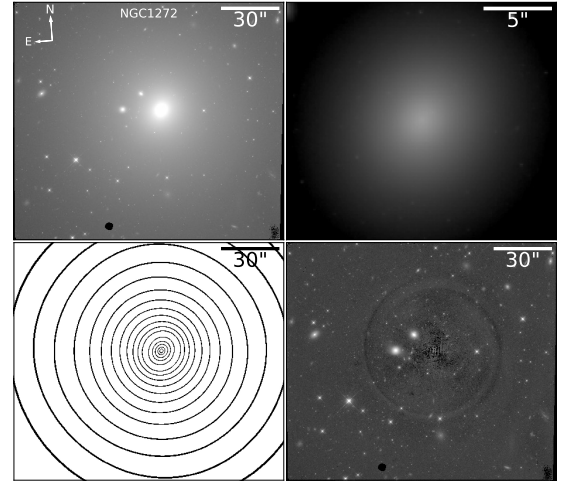
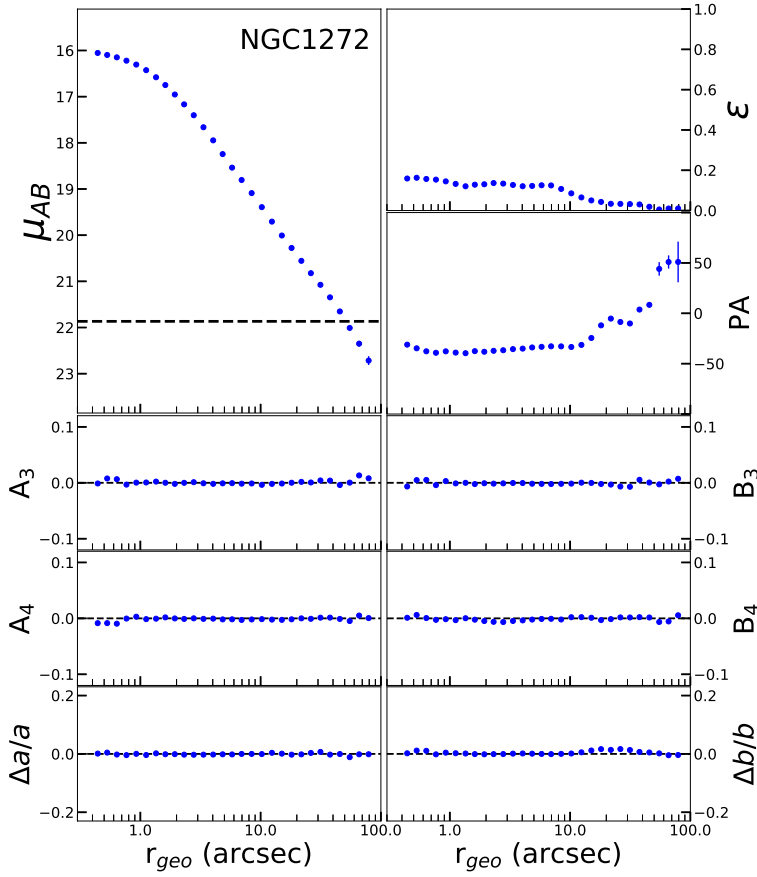


Figure 22. NGC 1272 features a large PA twist beyond ~ 10 arcsec that coincides with a steep decrease in the ellipticity, and the outermost isophotes are almost perfectly round. NGC 1272 has two small companions 15 and 21 arcsec northeast of the center. Scale: 1 arcsec = 376 pc.

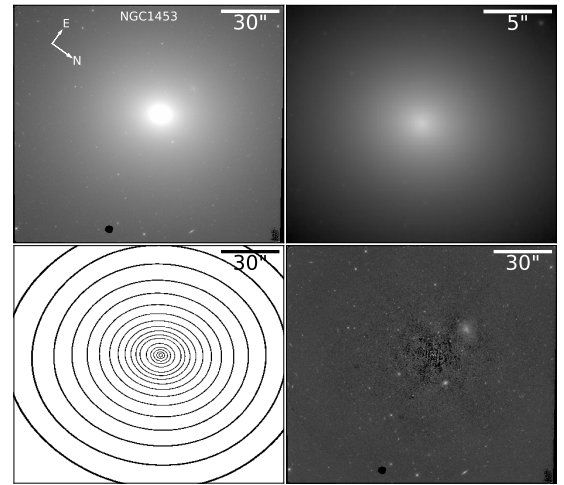
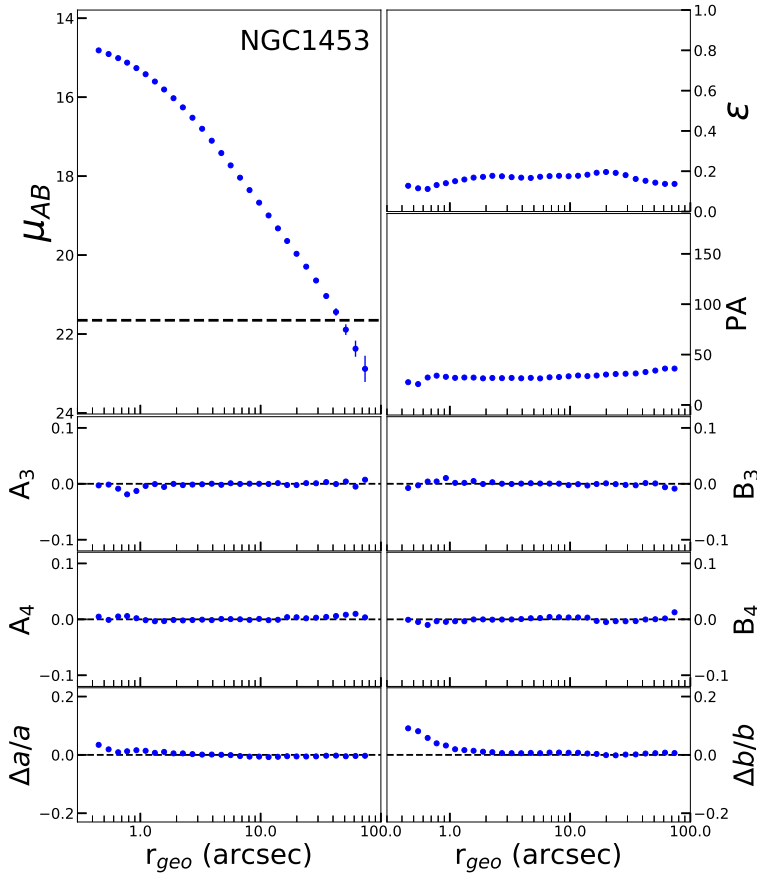


Figure 23. NGC 1453 has a noticeable central drift within ~ 0.6 arcsec. The extent of the drift is difficult to determine, as it is close to the resolution limit. The ellipticity varies only slightly. Scale: 1 arcsec = 273 pc.

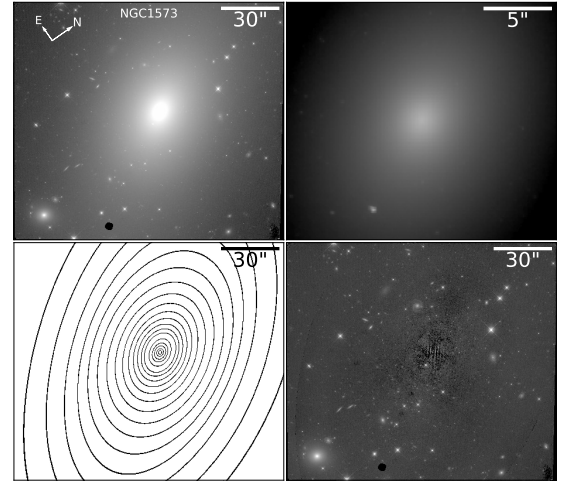
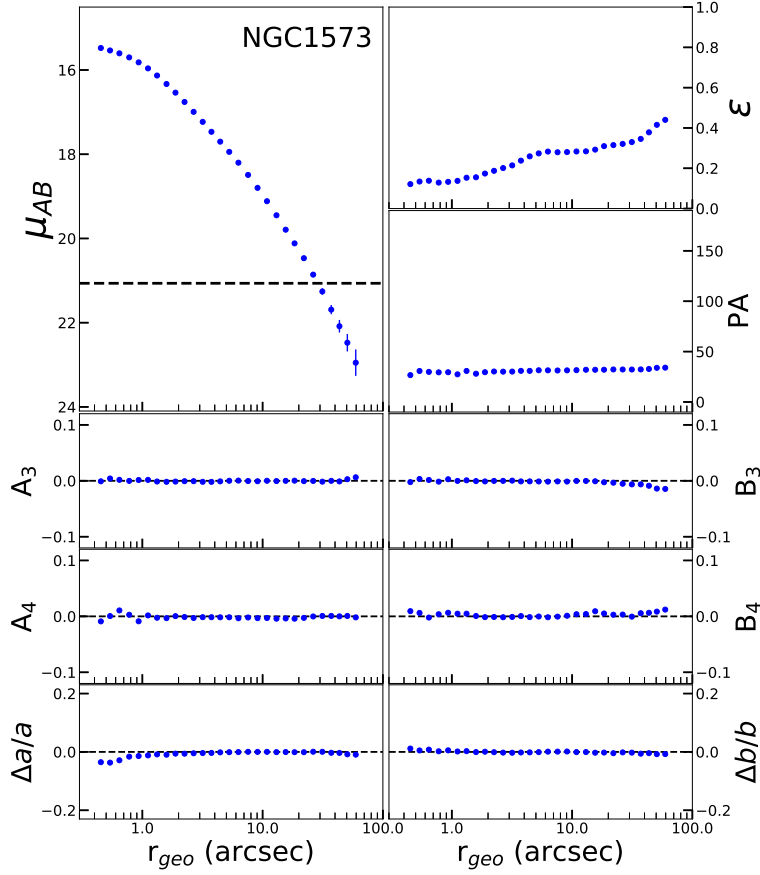


Figure 24. NGC 1573 has significantly increasing ellipticity with radius; the other parameters are fairly constant.
Scale: 1 arcsec = 315 pc.

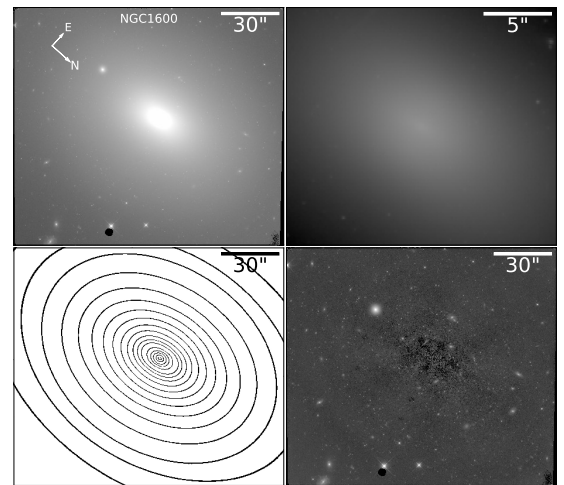
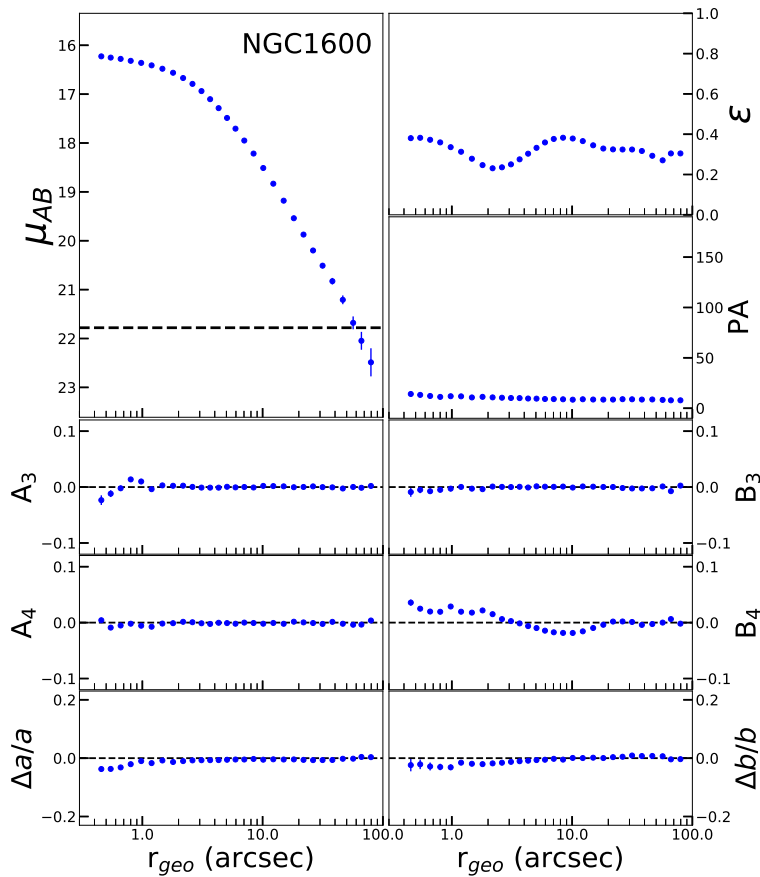


Figure 25. NGC 1600 has a variable ellipticity with an absolute minimum at ~ 2 arcsec. The inner isophotes are significantly disk-like, but transition to boxy isophotes around ~ 10 arcsec, beyond which they return to pure ellipticity.
Scale: 1 arcsec = 309 pc.

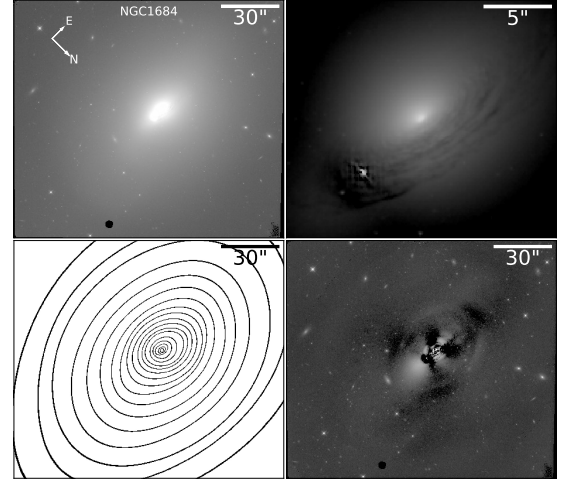
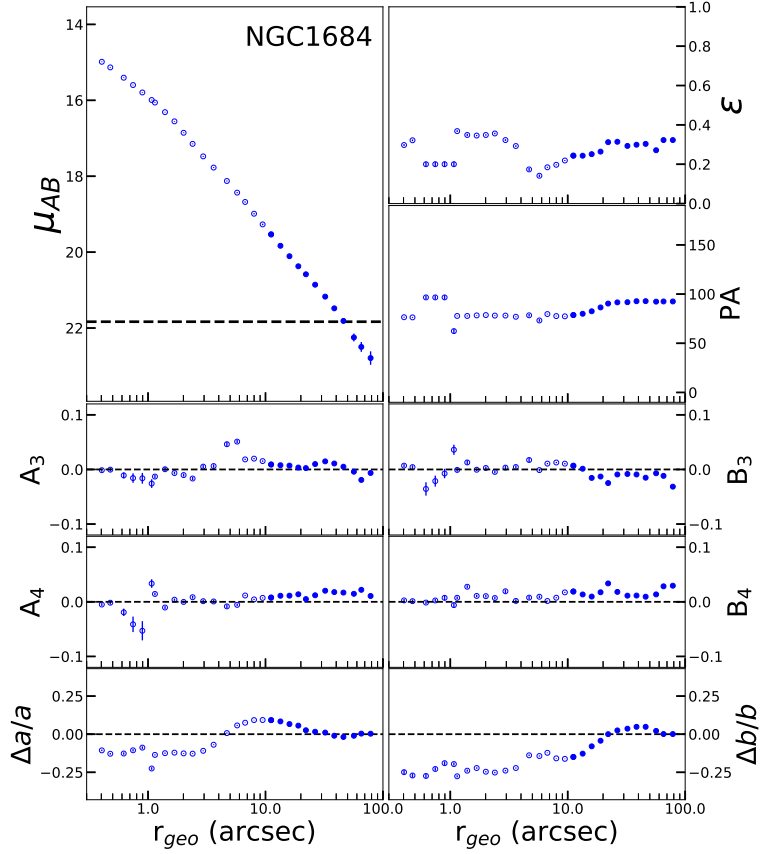


Figure 26. NGC 1684 has a central dust disk that distorts the isophotes within the central 11 arcsec. Outside of this disk, the isophotes are diskly. NGC 1684 has a small companion 6 arcsec west of the center. Scale: 1 arcsec = 308 pc.

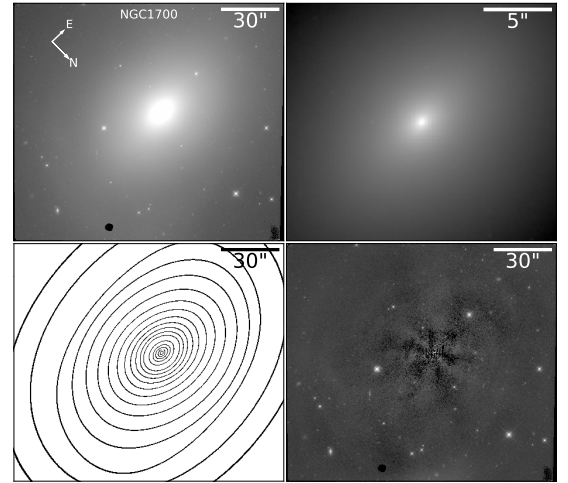
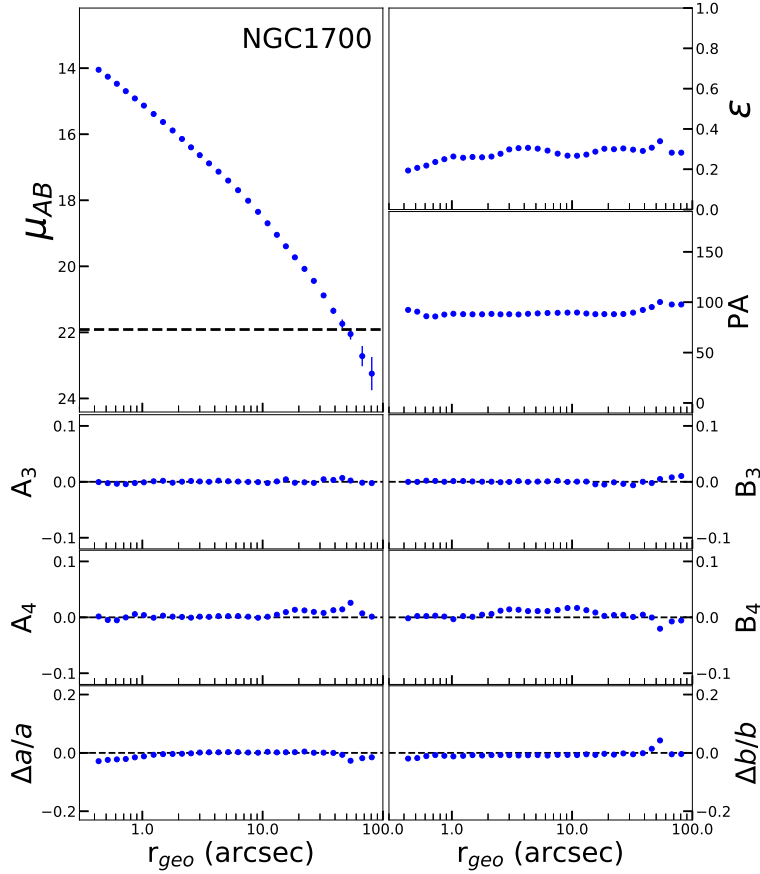


Figure 27. NGC 1700 has variable ellipticity that reaches a peak at ~ 4 arcsec. Beyond this value the ellipticity has small oscillations around ~ 0.3 . Between ~ 2 arcsec and ~ 12 arcsec the isophotes are diskly and elliptical otherwise. Scale: 1 arcsec = 264 pc.

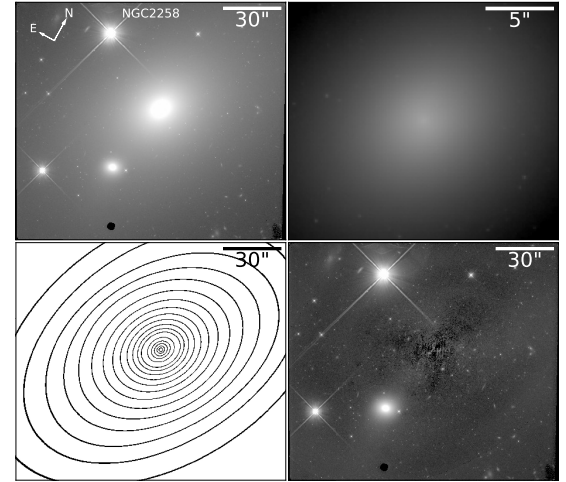
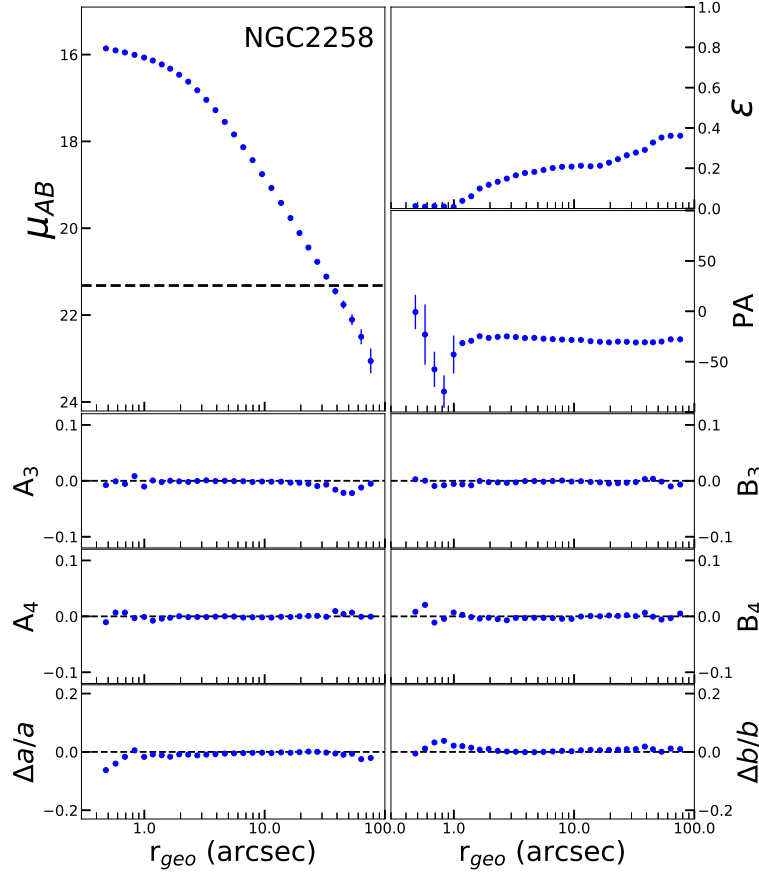


Figure 28. NGC 2258 has a small companion 39 arcsec to the south. Its ellipticity rises strongly with radius. Scale: 1 arcsec = 286 pc.

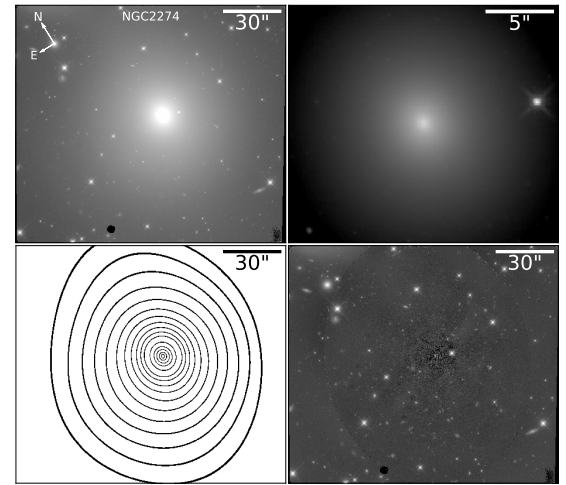
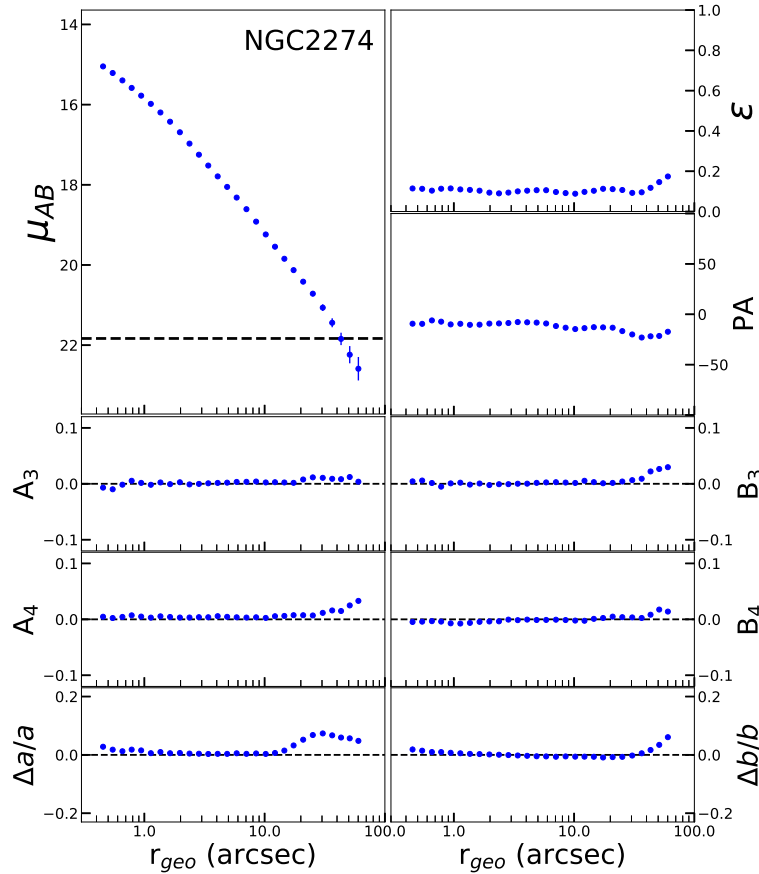


Figure 29. NGC 2274 has an extremely flat ellipticity, which remains at ~ 0.1 until ~ 30 arcsec, beyond which it rises to ~ 0.18 . The outermost isophotes become disk-like, corresponding to the radius where ellipticity increases. Beyond ~ 12 arcsec the isophote centers begin to drift, reaching a $\sim 5\%$ shift along the semi-major and semi-minor axes by the outermost isophotes. Scale: 1 arcsec = 358 pc.

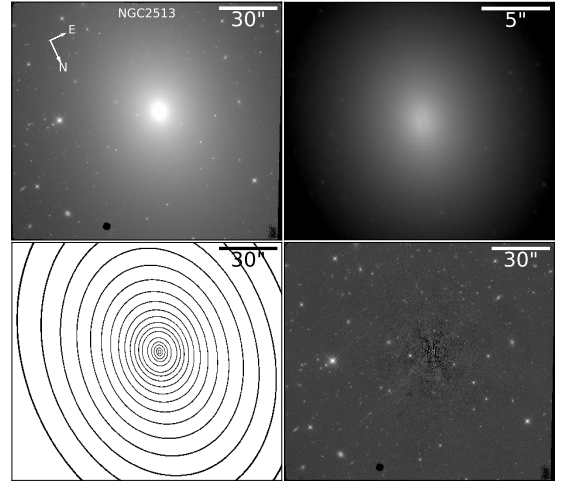
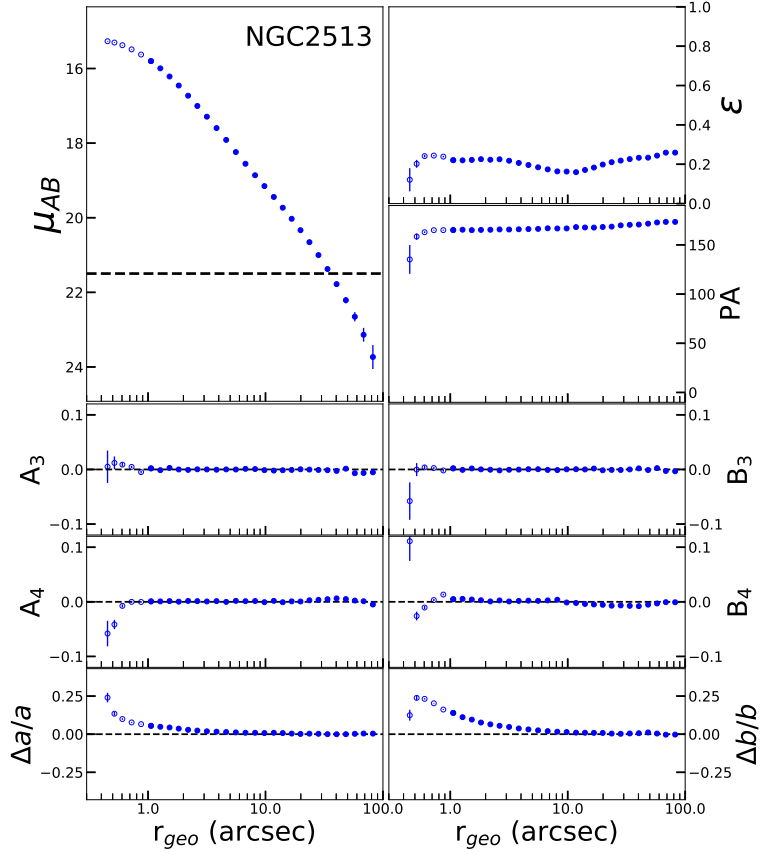


Figure 30. NGC 2513 has a small, compact dust disk that obscures isophotes within 1 arcsec. The ellipticity decreases to a minimum at ~ 10 arcsec, beyond which increases somewhat. Scale: 1 arcsec = 343 pc.

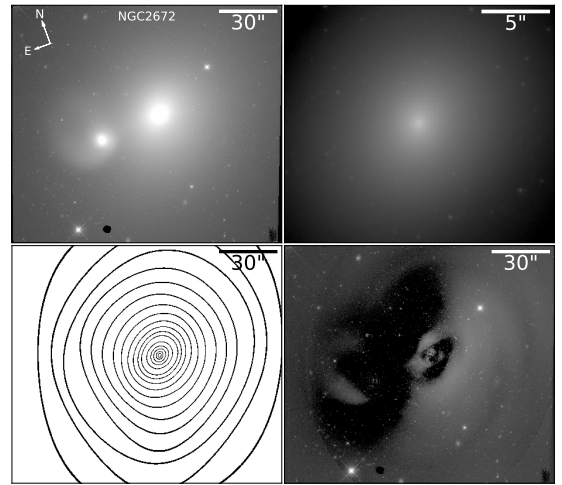
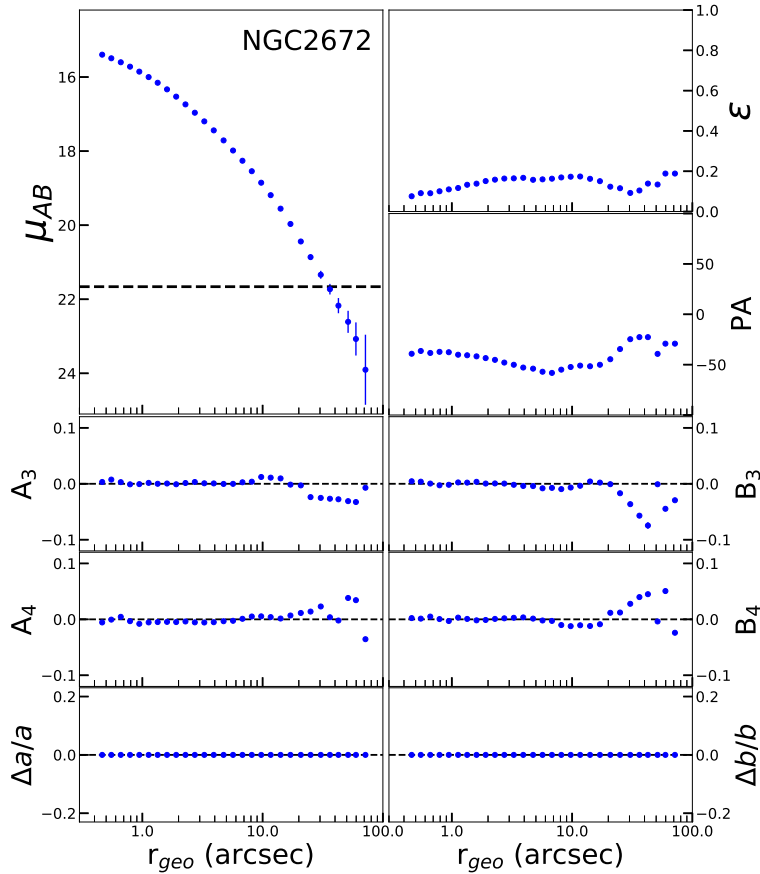


Figure 31. NGC 2672 has a large neighbor 33 arcsec east of its center. The tidal interaction of the two galaxies distorts the isophotes as follows: first, the ellipticity has a local minimum at ~ 33 arcsec. The PA, which is otherwise stable, has a noticeable jump as it approaches $r_{geo} \sim 33$ arcsec. The isophotes at this radius also become very disk-like because of the presence of the companion, but are boxy at other radii. Scale: 1 arcsec = 298 pc.

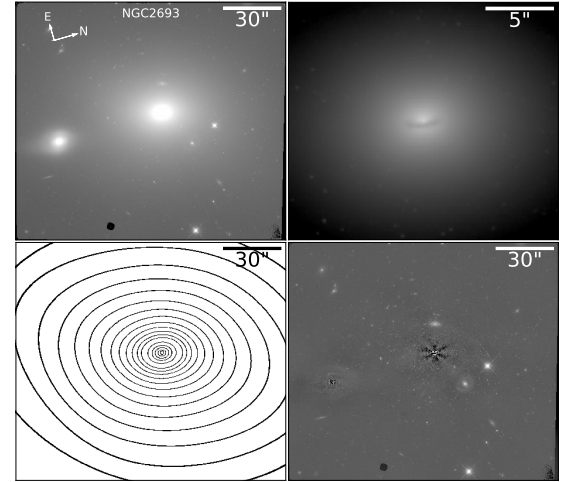
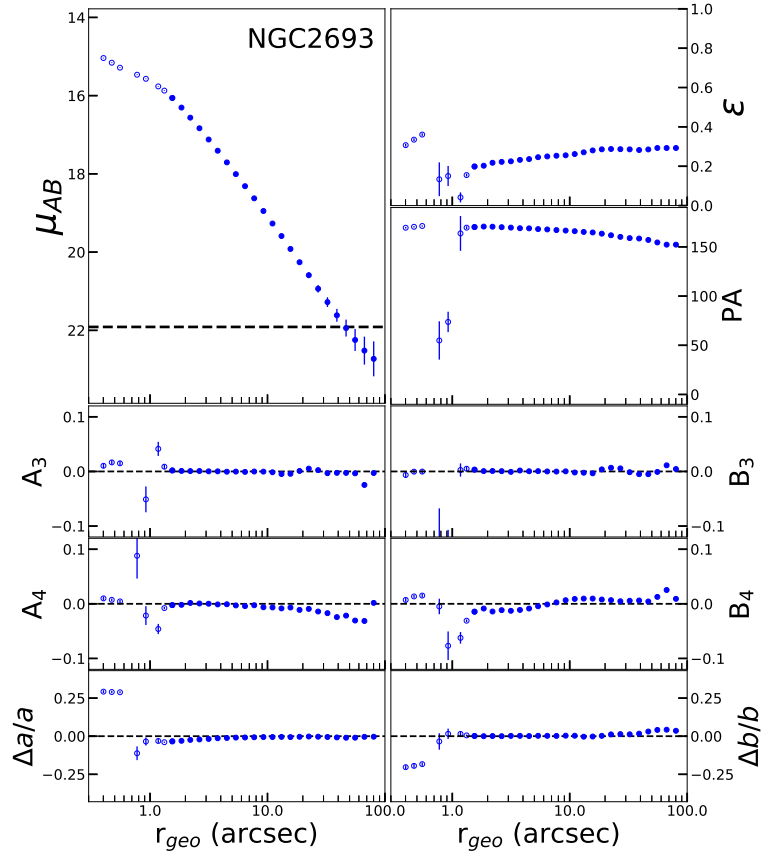


Figure 32. NGC 2693 has a small compact dust disk that extends 1.5 arcsec (radius) from the center. The inner isophotes are boxy, but become slightly disk-like beyond ~ 5 arcsec. NGC 2693 has a nearby companion 55 arcsec to the south. Scale: 1 arcsec = 361 pc.

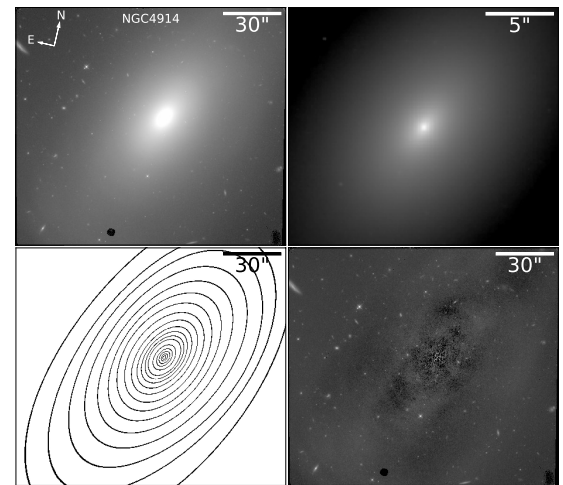
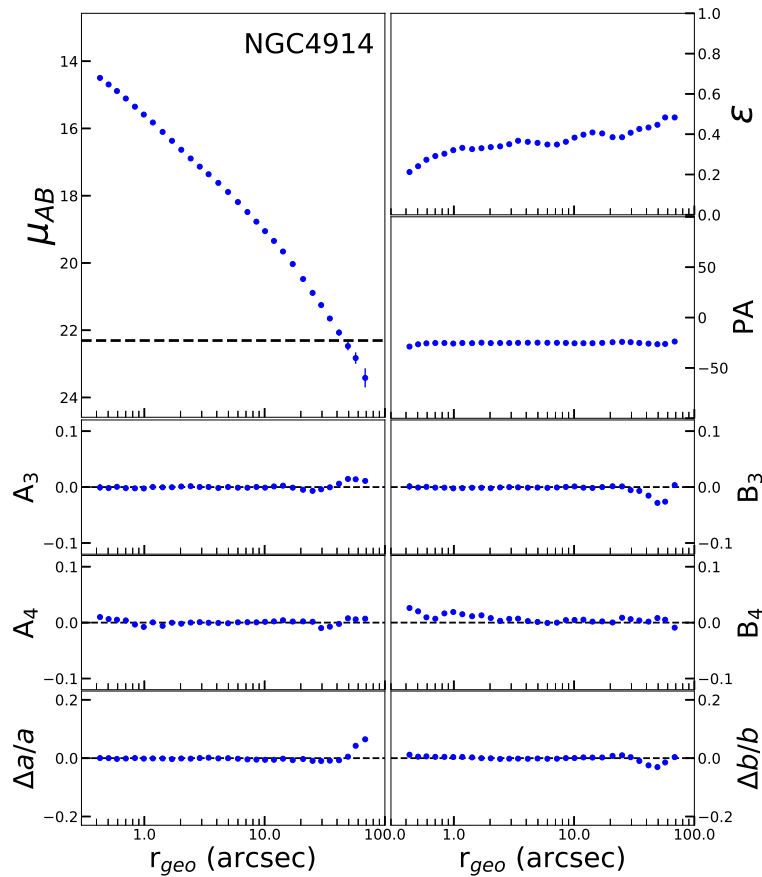


Figure 33. NGC 4914 has a steeply rising ellipticity profile, which reaches nearly 0.5 for the outermost isophotes. Isophotes are disk-like within ~ 1.5 arcsec and nearly elliptical farther out. Scale: 1 arcsec = 361 pc.

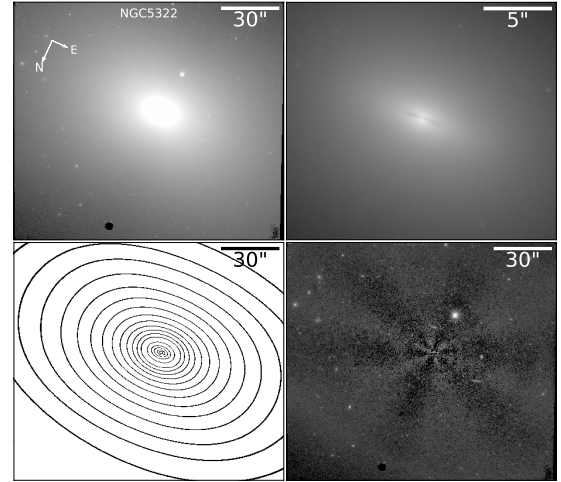
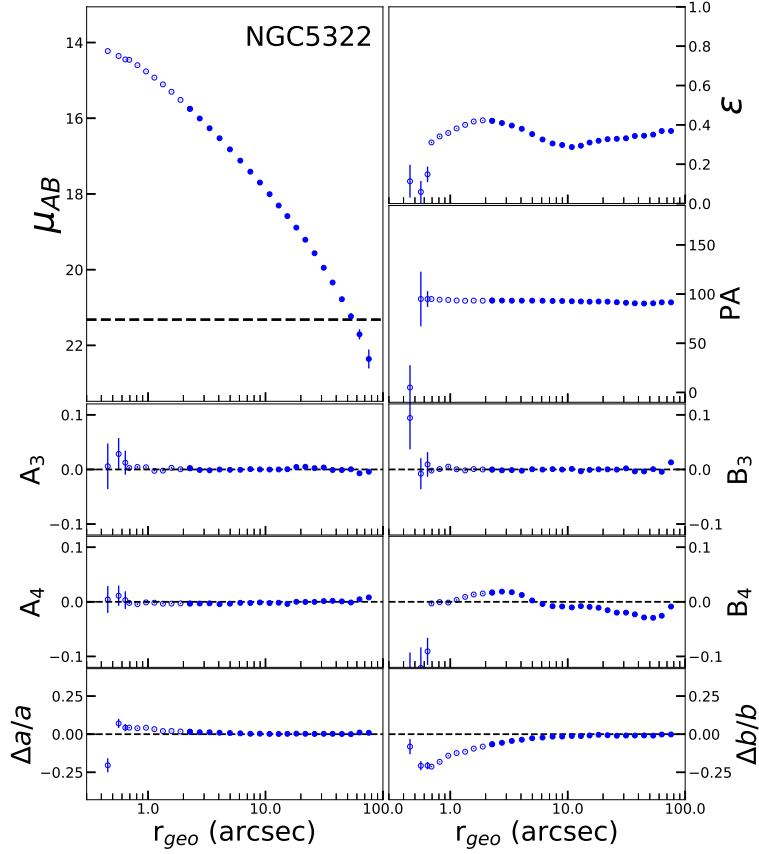


Figure 34. NGC 5322 has a small compact dust disk that extends 2 arcsec in radius from the center. The ellipticity reaches a maximum at the outer edge of the dust disk, and it decreases to a minimum at ~ 10 arcsec, beyond which it gradually rises. The isophotes at the edge of the dust disk are disky, but become more boxy with increasing radius. Isophotes beyond ~ 7 arcsec are significantly boxy. Scale: 1 arcsec = 166 pc.

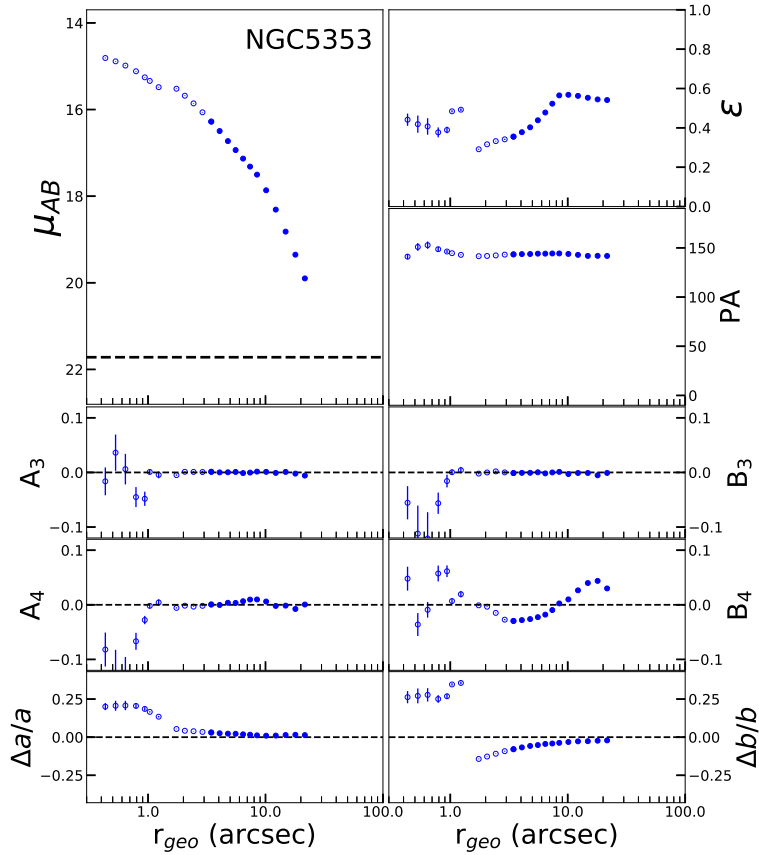


Figure 35. NGC 5353 has a dust disk that extends 3 arcsec from its center. It also has a large nearby neighbor to the north that is mostly off-frame. The outer isophotes are difficult to disentangle from the companion galaxy, and so isophotes beyond 25 arcsec are truncated. The ellipticity reaches a peak value of ~ 0.6 at a radius of ~ 10 arcsec, after which the ellipticity very gradually decreases. The isophotes between ~ 3 -8 arcsec are very boxy, but at ~ 10 arcsec this quickly shifts and the isophotes beyond ~ 10 arcsec are very disky. Throughout the dramatic shifts in isophotal shapes, the PA remains constant. Scale: 1 arcsec = 199 pc.

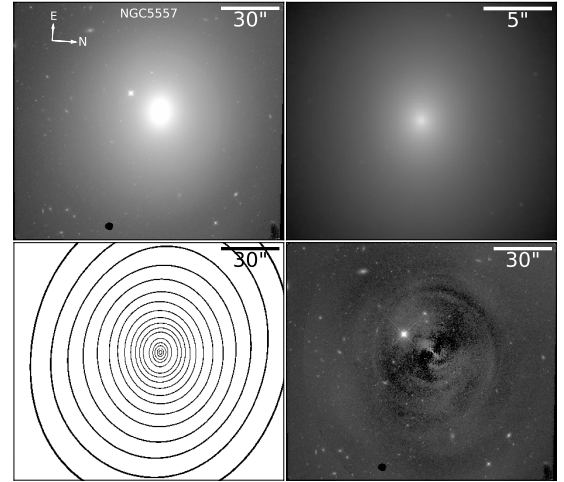
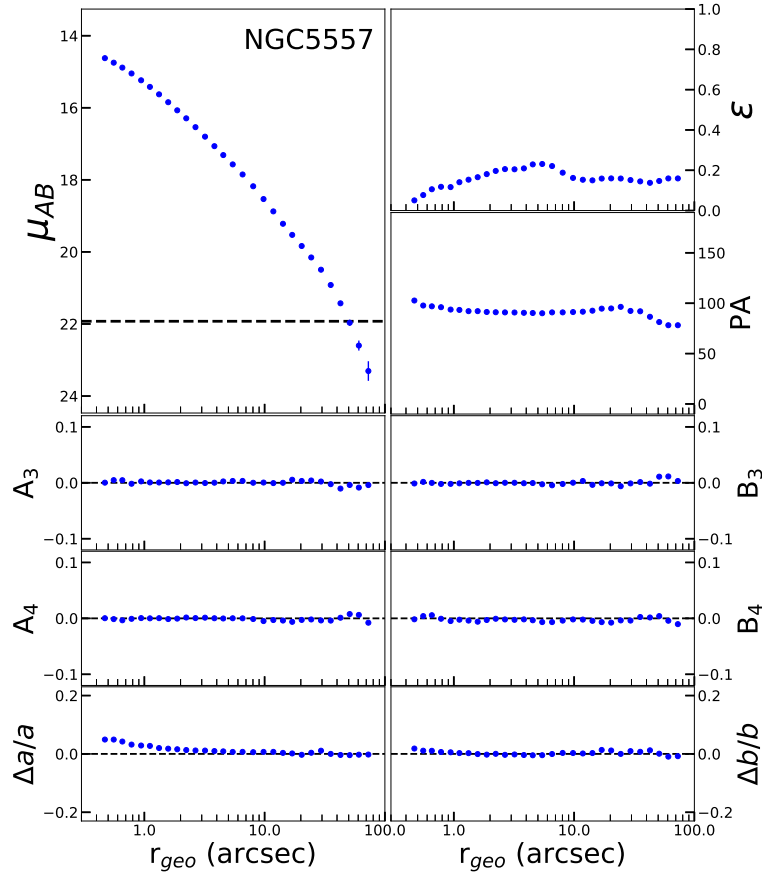


Figure 36. NGC 5557 has a small but varying ellipticity and modest PA shift at larger radii. It has a small companion to the southeast. Scale: 1 arcsec = 247 pc.

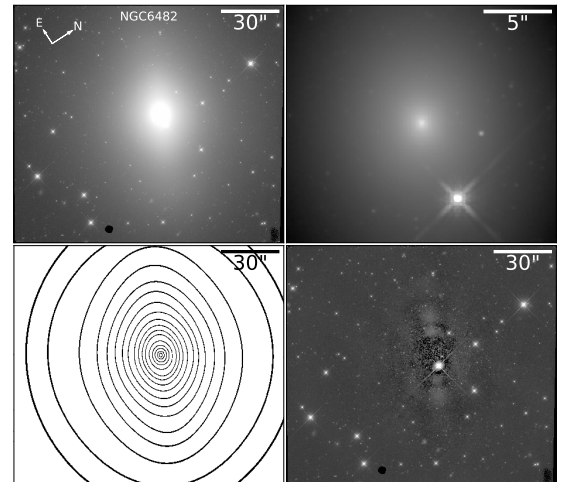
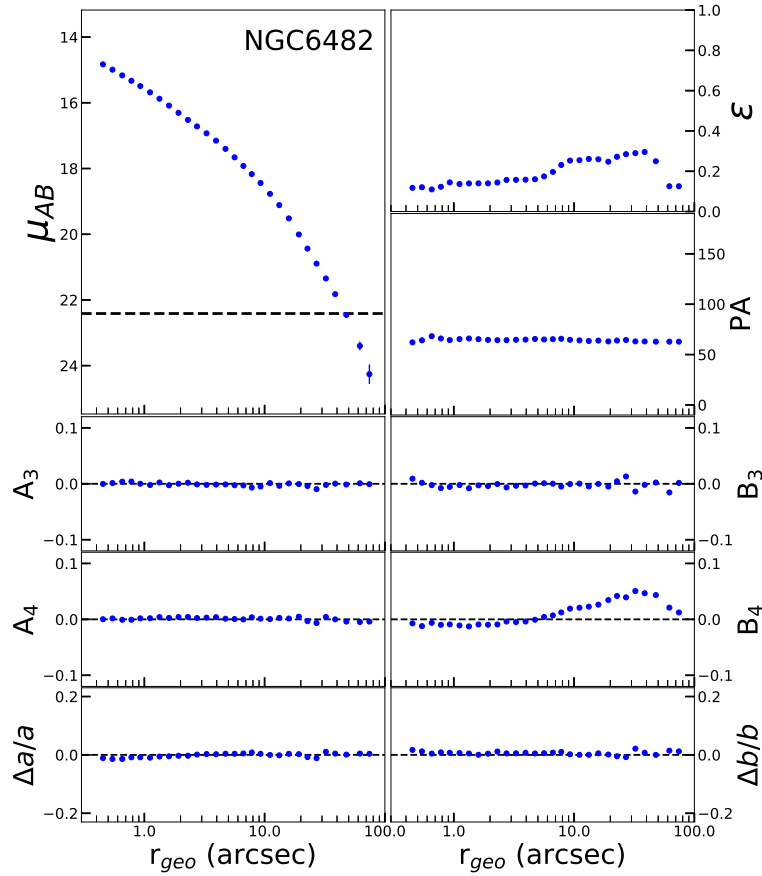


Figure 37. NGC 6482 has slightly boxy isophotes between ~ 0.5 and 2.5 arcsec. The isophotes become very disk-like beyond ~ 8 arcsec, but eventually become nearly elliptical (and round) in the outermost isophotes. Scale: 1 arcsec = 298 pc.

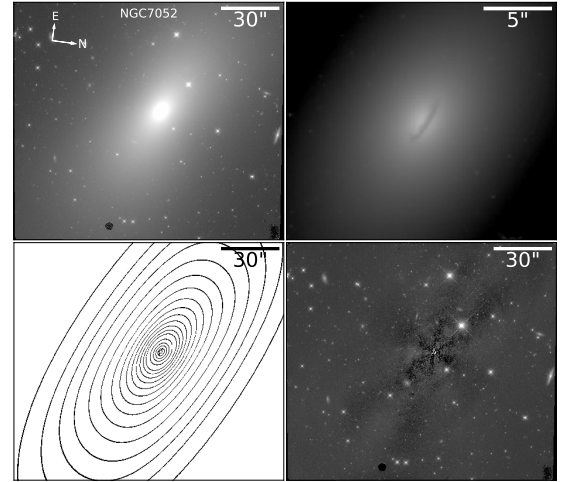
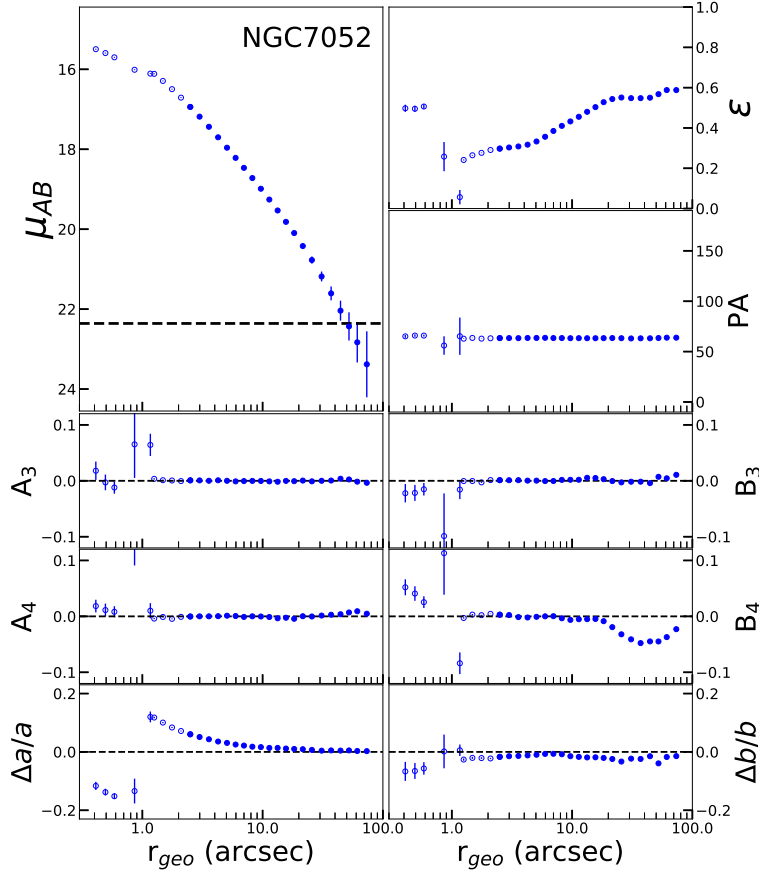


Figure 38. NGC 7052 has a compact dust disk that extends to a radius of 2 arcsec from its center. The ellipticity rises dramatically outside the dust disk, and reaches a peak of nearly 0.6 in the outermost isophotes. The isophotes beyond ~ 10 arcsec are very boxy. Scale: 1 arcsec = 336 pc.

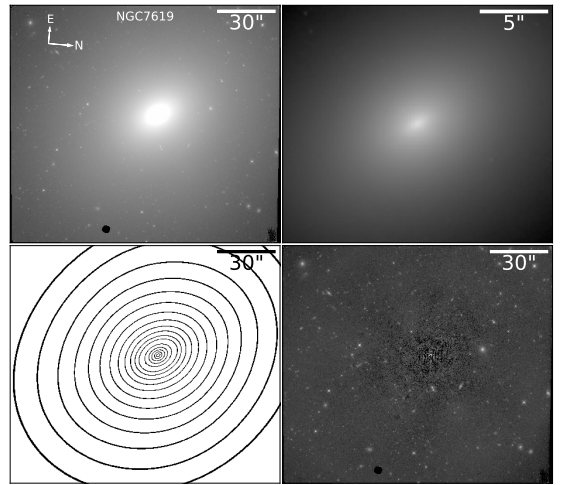
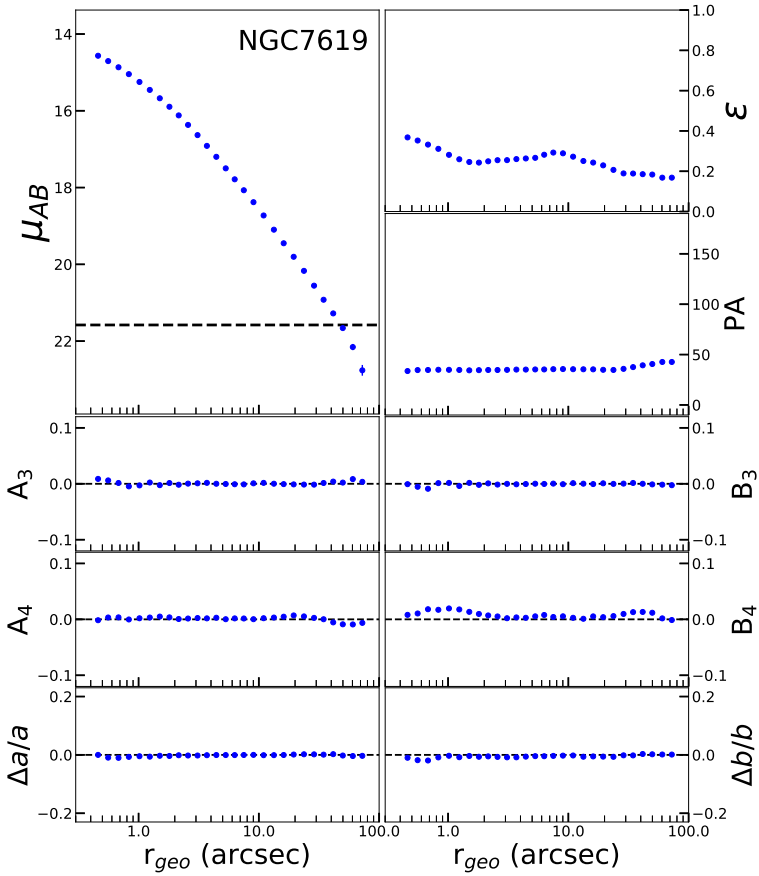


Figure 39. NGC 7619 has an ellipticity profile that decreases with increasing radius. The isophotes between ~ 0.6 to 2 arcsec and ~ 30 to 60 arcsec are slightly disk-like. Scale: 1 arcsec = 262 pc.